Posteromedial cortical networks encode visuomotor prediction errors

Authors

Ryosuke F. Takeuchi[1], Kei N. Ito,[1] Rumina Ueda,[1] Masahiro Yamaguchi,[1] Fumitaka Osakada[1,2,3,4,5]*

Affiliations

[1]Laboratory of Cellular Pharmacology, Graduate School of Pharmaceutical Sciences, Nagoya University, Nagoya, Japan

[2]Laboratory of Neural Information Processing, Laboratory of Neural Information Processing, Institute for Advanced Research, Nagoya University, Nagoya, Japan

[3]Institute of Nano-Life-Systems, Institutes of Innovation for Future Society, Nagoya University, Nagoya, Japan

[4]Institute for Glyco-core Research, Nagoya University, Nagoya, Japan

[5]PRESTO/CREST, Japan Science and Technology Agency, Saitama, Japan

*Correspondence author: Fumitaka Osakada, Ph.D.

Laboratory of Cellular Pharmacology, Graduate School of Pharmaceutical Sciences, Nagoya University, Japan

Tel: +81-52-747-6814

Fax: +81-52-747-6815

E-mail: fosakada@ps.nagoya-u.ac.jp

Abstract

The purpose of sensory processing in the brain involves guiding animals to appropriate actions by estimating the causes of sensory changes in the environment. Encoding prediction error computed from the mismatch between actual input and predictions based on experience is considered an effective strategy for sensory perception in the brain. However, it remains unknown how predictive computation is implemented in the hierarchy of neural circuits in cortical areas. Here, we monitored dorsal cortex-wide neural activity using a wide-field Ca^{2+} imaging technique when mice encountered visuomotor mismatches in virtual reality. Posterior medial cortical areas sequentially responded to the visuomotor mismatches. The magnitude of these responses was associated with the predictability of the mismatch events. Granger causality and anatomical analysis demonstrated experience-dependent information flow structure underlying the mismatch signal transmission across the cortex. Our results reveal that the subnetworks in posteromedial cortical areas process the prediction errors in a hierarchical manner.

Introduction

Changes in sensory inputs arise from the external environment and self-movements, such as eye movements, head-orienting movements, and locomotion. Distinguishing between environmental changes and self-generated sensory input is essential for animal sensory perception and action. The brain detects unpredicted changes in sensory input as a mismatch between animal's internal predictions and actual sensory inputs to differentiate whether the input is self-generated or environmentally generated [1,2]. In the predictive coding theory, predictions of future sensory inputs are transferred as top-down signals from higher to lower areas in the hierarchy, whereas bottom-up signals from lower to higher areas encode prediction errors–differences between predictions and sensory inputs [3,4]. The predictive coding theory postulates a hierarchical organization of cortico–cortical communications; however, it remains unknown how predictive coding is implemented in the hierarchy of neural circuits in the brain.

In the primate visual system, many lines of evidence have demonstrated parallel and hierarchical processing of visual information [5,6]. The processing of visual information is initiated in the retina, sent to the lateral geniculate nucleus, and relayed to the primary visual cortex (V1). V1 neurons send its output to a hierarchical series of extrastriate visual areas [7], which organize two ventral and dorsal visual information processing streams, representing a variety of visual features related to object perception and spatial perception [8–10]. Recent studies have revealed that the mouse visual system also uses parallel and hierarchical processing strategies [10,11], suggesting the existence of ventral and dorsal visual processing streams in mice [12]. However, it remains elusive how these cortical areas are functionally segregated with respect to behaviorally relevant features. By contrast, in sensorimotor processing, the copy of the motor command is sent to other areas of the brain as a corollary discharge. Previous studies demonstrated that top-down signals transmitted from movement-related areas are integrated in lower-level sensory areas [13–16]. In

particular, subpopulations of V1 neurons compute visuomotor prediction error by utilizing top-down, locomotion-related signals [13,17–20]. However, it is unclear whether other cortical areas outside of the V1 contribute to predictive processing for visual perception during movement in an experience-dependent manner and how those areas interact with the V1.

In the present study, we addressed how visuomotor prediction errors are encoded in the hierarchy of neural circuits in the mouse brain. We used a virtual reality (VR) environment to present visuomotor mismatches between predicted and actual visual feedback to head-fixed mice. Using wide-field imaging from mice with expression of the Ca^{2+} indicator jGCaMP7f in pan-excitatory neurons, we found that posteromedial cortical areas, including the V1, retrosplenial cortex (RSP), posteromedial visual cortex (PM), and anteromedial visual cortex (AM) significantly responded to the visuomotor mismatches induced by artificial perturbation of the visual flow in the VR. The mismatch responses in those areas were modulated by the predictability of the mismatch event. Granger causality analysis revealed a directed information flow of the mismatch between cortical areas at different hierarchical levels. Combined with anatomical analysis for axonal projections, these results indicate that a subnetwork comprising V1, higher visual areas, and RSP in the dorsal cortex conveyed visuomotor prediction error signals. Thus, the present study provides experimental evidence of the distributed and hierarchical organization underlying predictive coding in visuomotor integration.

Results

Wide-field Ca^{2+} imaging of excitatory neural network in the dorsal cortex

We aimed to record the macroscopic activity of excitatory neurons across the dorsal cortex as broadly as possible. We intravenously injected blood–brain barrier-permeable adeno-associated virus (AAV) vectors expressing jGCaMP7f under the excitatory-neuron-specific CaMKII promoter (AAV-PHP.eB-CaMKII-jGCaMP7f) into the mouse retro-orbital sinus. jGCaMP7f-expressing cells were distributed throughout the cortex, striatum, hippocampus, and cerebellum[21,22]. Most jGCaMP7f-expressing neurons in the cortex showed a typical morphological feature of pyramidal cells and were distributed across layers in the V1, lateromedial visual area (LM), PM, and dorsal and lateral agranular parts of the RSP (RSPd and RSPagl, respectively) (Fig. 1a; percentage of L1–3/L4–6, V1: 32.7%; LM: 30.8%; PM: 39.6%; RSPd: 25.8%; RSPagl, 34.9%). To test the viral infection specificity toward excitatory neurons, we performed immunostaining for the inhibitory neuron subtype markers parvalbumin (PV), somatostatin (SOM), and vasoactive intestinal peptide (VIP). Few jGCaMP7f-expressing neurons in the V1 and the secondary motor area (M2) were positive for these inhibitory neuron markers (Fig. 1b; PV: 2.2%; SOM: 1.3%, VIP: 0.0% in V1; PV: 1.1%; SOM: 0.5%; VIP: 0.4% in M2). Thus, intravenously delivered AAV-PHP.eB-CaMKII-jGCaMP7f efficiently introduced jGCaMP7f into excitatory neurons across the cortex.

We then measured dorsal cortex-wide neural activity of AAV-PHP.eB-CaMKII-jGCaMP7f-injected mice using the wide-field Ca^{2+} imaging technique. The fluorescent signal of cortical neurons expressing jGCaMP7f was measured through the cleared skull using a custom-built macroscope. We used alternate multiwavelength excitation methods of jGCaMP7f (temporal multiplexing of 405 and 470 nm LEDs, Fig. 1c and Supplementary Fig. 1) to filter the Ca^{2+}-independent fluorescent intensity change [23–25]. We used linear fitting correction to filter intrinsic

autofluorescence and other artifactual signals. The correction procedure successfully canceled the negative fluorescent changes through intrinsic signals in response to visual stimuli (Supplementary Fig. 2, Supplementary Movie 1). The acquired images were semi-automatically aligned to the top view of Allen Common Coordinate Framework (ACCF) for the mouse brain [26], based on two anatomical control points (Fig. 1d). To validate the alignment quality with functionally defined maps, we performed retinotopic mapping and resting-state connectivity mapping. Head-fixed mice were subjected to retinotopic mapping with periodically moving checkerboard visual stimuli. We computed a visual field sign map to match the border across visual areas to that in the ACCF (Fig. 1e). Moreover, we examined whether neural responses from a large part of the cortex could be obtained with wide-field Ca^{2+} imaging. The signal-to-noise ratio (S/N) to the visual stimulus was comparable across the dorsal cortex, and even across lateral visual areas from PM to LM (Fig. 1f). To further validate the registration, we performed seed-based correlation analysis for resting-state activity data. Regions of interest (ROIs) were set in the V1, LM, anterolateral visual cortex (AL), PM, AM, rostrolateral visual cortex (RL), posterior and anterior parts of the RSP (RSPp and RSPa, respectively), and the medial and anterior M2 (M2m and M2a, respectively) (Fig. 1G and Supplementary Fig. 3b). Based on studies focusing on functional architecture of RSP [27–29], we set two distinct ROIs in RSP. We also confirmed the differential anatomical inputs and outputs between RSPp and RSPa with retrograde and anterograde tracing (Supplementary Fig. 3). The structure of high-correlation coefficient pixels of these maps was matched to the areal compartment of the ACCF. Furthermore, to extract functionally segregated groups of pixels, we applied principal component analysis to resting-state neural activity. The spatial patterns of major principal components were highly matched to the areal compartments of the ACCF (Supplementary Fig. 4). Therefore, wide-field Ca^{2+} imaging and subsequent alignment to the ACCF allowed functional analysis of neural dynamics at a dorsal cortex-wide and inter-areal scale.

Visuomotor feedback mismatch evokes distributed and sequential activities in the posteromedial cortex

To explore neural responses to visuomotor prediction errors, we recorded the dorsal cortex-wide neural activity of mice in one-dimensional VR [13]. Animals were head-fixed and free to run on a treadmill surrounded by three monitors that provided visual flow with a random corridor texture on virtual walls (Fig. 2a−c. The visual flow speed was coupled to the locomotion speed of the mouse under the normal closed-loop condition (Supplementary Movie 2). Mice were reared under normal light-dark cycles in their home cage to make all their visuomotor experiences "coupled". Prior to an imaging session, the mice were habituated to the VR (3–5 sessions, ~5 h in total, without mismatch event) to experience the relationship between their locomotion on the treadmill and the visual feedback flow speed of the VR [13,18]. During the imaging session, face images were recorded to monitor the mouse's behavior (Fig. 2b). We quantified behavioral responses, such as blinking, pupil dilation, saccadic eye movement, and running speed (Supplementary Fig. 5). Mice were free to run during the entire imaging session and showed spontaneous voluntary locomotion and eye movement (Fig. 2c). This paradigm allowed us to present unexpected visual feedback perturbation to mice running in the VR. Herein, we defined a mismatch between self-generated predicted visual input and actual perturbated visual input as a visuomotor mismatch.

We presented visuomotor mismatches to the mice in the VR environment by brief visual feedback perturbation (1.5 s) at random timing, independent of the locomotion speed (Fig. 2c, event possibility = 5.5% /s, absolute refractory period = 4.0 s). Trials when mice exhibited blinking, grooming, or low locomotion on mismatch onset were excluded from the analysis (locomotion speed threshold = 3.0 cm/s). The visuomotor mismatches caused widespread and sequential cortical activities (Fig. 2d–h, Supplementary Movie 3 and 4). We found determinate changes in

the fluorescent signal from the medial parts of the visual areas. The response magnitude was highest in PM; however, V1 and RSPp peaked faster than PM, AM, and A (Fig. 2f–h, $p < 0.01$, Signed–Rank test). Distinctive positive peak responses were not detected in RL and lateral visual areas, such as AL and LM (Fig. 2g). Pupil dilation responses to the mismatch events were observed (Supplementary Fig. 5), consistent with previous studies[30,31]. As a control, we introduced green fluorescent proteins (GFP) instead of jGCaMP7f in mice by AAV-PHP.eB-hSyn-GFP injection and subjected them to wide-field imaging. GFP-expressing neurons across the cortex did not show such mismatch response patterns (Supplementary Fig. 6). Thus, these activity maps illustrate the sequential response of the visuomotor mismatch signals in the posteromedial cortical areas.

We then investigated whether each cortical area encodes the degree of prediction error. A previous study showed that the trial variance of the mismatch response in V1 reflected the degree of the visuomotor prediction error [13,30]. Accordingly, the magnitudes of the errors and neural responses are expected to be positively correlated. We analyzed the linear relationship between the response magnitude and mismatch magnitude, which corresponds to the average locomotion speed before and after mismatch onset (−250 to 250 ms, threshold = 0.01 cm/s). The response magnitude (average of 0.0 to 0.5 s from mismatch onset) in the medial higher visual areas (HVAs) such as PM and AM were significantly correlated with locomotion speed (Fig. 2i−j). However, parietal association areas such as RL and A did not show significant correlations with the mismatch (Fig. 2i−j). Notably, the mismatch response magnitude of RSPp was significantly correlated with locomotion speed, whereas the response magnitude of RSPa was not (Fig. 2j, RSPp: $p = 0.002$, RSPa: $p = 0.951$). These results suggest that the posteromedial cortex, such as PM, AM, and RSPp, encoded the occurrence and degree of visuomotor prediction errors.

Locomotion-related signals *per se* do not account for the mismatch response

Next, we tested the possibility that purely motor responses to mismatch events could account for the variability in cortical responses. Physiological and theoretical studies suggest that visuomotor prediction error signals are computed as comparisons between locomotion-related top-down signals and visual-flow-speed bottom-up signals [17,18]. Reportedly, movement-related signals widely evoked cortical activities, even in early sensory areas [25,32–34]. To determine whether the locomotion speed of mice accounted for the mismatch responses, we performed the multiple linear regression analysis, with the object variable as the neural response of each ROI. Explanatory variables were the locomotion speed during mismatch onset (−250 to 250 ms) and the change of locomotion speed at the peri-onset of the mismatch event (−250 to 0 to 0 to 250 ms). *t*-Statistics of the pre-locomotion speed were significant ($p < 0.05$) for V1, PM, AM, and RSPp (Supplementary Table. 1). By contrast, *t*-statistics of changes in the locomotion speed (ΔSpeed) in those areas were not significant, given the other terms in the linear model. However, among the more anterior areas, such as S1ll, A, and RSPa, the contribution of speed change (ΔSpeed) was statistically significant ($p < 0.05$). These results suggest that the locomotion speed change *per se* less contributes to the mismatch neural response in posterior cortical areas than the degree of the prediction errors does.

To evaluate whether locomotion-related signals are conveyed to the posterior cortical networks, we carried out Ca^{2+} imaging on mice in the dark without visual input changes from their locomotion (n = 5 mice, same subjects as in Fig. 2, Supplementary Movie 5 and 6). Many dorsal cortical areas significantly responded to locomotion onset in the dark, and the response magnitudes significantly varied between cortical areas (Fig. 3a). In the frontal and temporal areas, S1ll (corresponding to the caudal forelimb area) showed a large and reliable response at locomotion onset, whereas M2a showed little response. In posterior areas, many visual areas responded to

locomotion onset in the dark. However, RL showed a significantly lower response to locomotion onset than other visual areas (Fig. 3b, $p < 0.01$, permutation−test). Notably, RL also showed a small response to visuomotor mismatch (Fig. 2d−j). These results suggest that V1, PM, AM, and RSPp, which showed marked responses to the visuomotor mismatches, receive motor-related signals during locomotion, and can utilize these signals to encode sensorimotor prediction errors.

Prior experiences affect the visuomotor mismatch response in the cortex

We next examined whether the "predictability" of mismatch events accounts for the activity in the posteromedial cortical networks. We compared the neural response to "predictable" visuomotor mismatch events with that to "unpredictable" visuomotor mismatches at the identical locomotion speed of animals. In the semi-closed-loop VR (SCL-VR), the visual flow feedback perturbation was triggered when the locomotion speed exceeded the threshold of 6.0 cm/s (refractory period = 4.0 s, locomotion speed calculation time window = 1.0 s). Unlike the normal mismatch experiments where mismatches were presented at random timing (Fig. 2), the visual feedback perturbation timing in the SCL-VR is predictable for the mismatch-experienced group (ME group) trained in the SCL-VR. However, the visual feedback perturbation timing in the SCL-VR is unpredictable for the normal-VR-experienced group (NE group) trained in the regular closed-loop VR as a control. Because visuomotor mismatch response mainly arises from the prediction error formed by prior experiences during the habituation sessions, the response magnitude in the NE group is expected to be larger than that in the ME group under the conditions of the same visual flow speed change at the same locomotion speed (Fig.4c).

First, to examine how experiences in the SCL-VR affect the predictability of mismatch events, we quantified the behavioral mismatch response[17]. During the VR habituation sessions, each mouse was trained either in the regular closed-loop VR or in the SCL-VR (Fig. 4a). Mice

were trained for 5 consecutive days before the imaging session (Fig. 4b, 6.5 hours in total). At the imaging session, the average locomotion speed in the early phase of mismatch periods (0.0 to 1.2 s) was not statistically discriminable between NE and ME groups (Fig. 4d, e, and Supplementary Fig. 7). Thus, the property of visual feedback halt and self-locomotion speed is comparable between the NE and ME groups before and after the mismatch onset. In the late phase of mismatch periods (1.2 s–), the locomotion speed of the NE group was significantly slower than that of ME mice. Pupil dilation of the NE group was significantly larger than that of the ME group (Fig. 4e and Supplementary Fig. 7). These results suggest that the ME group acquired the prior information based on the habituation in the SCL-VR and showed less surprise to the self-induced mismatch event than the mismatch-unexperienced NE group.

We further compared the neural responses to the self-induced mismatches between the NE and ME groups with wide-field Ca^{2+} imaging. In both groups, spatiotemporal patterns of neural responses were similar (Fig. 4f). Positive mismatch responses were observed among wide regions of the dorsal cortex, such as M2m, RSPp, RSPagl, AM, and PM (Fig. 4g–h) in both groups of animals. The difference in the response magnitude during the early period of the mismatch (0.0 to 0.75 s) between the NE and ME groups was statistically significant in visual areas (V1, PM, and AM), RSPp, RSPagl, and M2m (Fig. 4i–j). Consistent with the results in the random mismatch VR (Fig. 2f–j), the response in RL during the periods was small and the difference between the NE and ME groups in RL was relatively small during the periods (Fig. 3h). These results indicate that the visuomotor mismatch responses observed in the posterior medial cortical areas were formed largely by prediction errors.

Mismatch responses in posterior cortical areas decrease after visuomotor experiences in VR

From the results demonstrating that mismatch response magnitude was lower in the ME group than in the NE group (Fig. 4), we conceived that subsequent visuomotor mismatch experiences in the NE group should reduce their mismatch response magnitude. To test this possibility, we subjected the same set of the NE mice (Fig. 4) to habituation to predictable visuomotor mismatches in the SCL-VR after the first recording session, then recorded the neural and behavioral mismatch responses from these mismatch-experienced NE mice (Fig. 5a, Supplementary Table 2). The running speed constancy was higher in the second session than those in first session; pupil dilation in response to the visuomotor mismatches was lower in the second session than in the first session (Fig. 5b−c). Notably, the neural responses in V1, PM, and RSPp to the mismatch decreased after the subsequent experiences in the SCL-VR (Fig.5d−e). These results support the conclusion that prediction error components drive the mismatch response activities in the posterior medial cortical areas.

A medial dorsal stream subnetwork propagates mismatch signals

Given the framework of predictive coding, the observed macroscopic neural activity patterns by visuomotor mismatch across the dorsal cortex suggest the hierarchical propagation of prediction error signals [3,35]. To examine specific information flow of the error signals between cortical networks, we compared the overall magnitude of activity correlation between ROIs when mice were in the resting-state, stationary, or running in the dark (Supplementary Movie 1, Supplementary Fig. 5 and 6), under the closed-loop period in the regular closed-loop VR (−1.5 to 0.0 s from mismatch onset), and under the feedback mismatch periods in VR (Fig. 6a−b, Supplementary Fig. 8a) [33,36]. Mice that were anesthetized, stationary, or running in the dark showed

more globally correlated activities between areas. Notably, the correlation coefficients between V1−RSPp, RSPp−PM, V1−PM during the mismatch period were significantly higher than those in the closed-loop period (Fig. 6b and Supplementary Fig. 8b, $p < 0.01$). These effects suggest context-dependent modulation of cortico–cortical communications, which underlies the processing of visuomotor prediction errors.

To examine the hierarchical relationship among cortical areas, we next conducted conditional Granger causality (GC) analysis [29,37,38] on activity recorded during the closed-loop and mismatch periods, which allows for the examination of directed functional interactions between cortical areas. The structure of GC magnitudes of the cortex under these contexts differed between closed-loop and mismatch conditions (Fig. 6c), which is consistent with the correlation analysis (Fig. 6a−b). The mismatch period showed large GC from V1 and RSPp to the posterior areas, such as PM, AM, and RSPa. By contrast, the closed-loop condition did not show significant GC magnitude from V1 to other HVAs, parietal areas, and RSP, although the visual flow speed dynamically changed during the closed-loop. Additionally, the GC magnitude from RSPp to V1 and other dorsal cortical areas was larger than that from V1 to RSPp during mismatch periods. These results point to a large information flow from V1 and RSPp to HVAs during mismatch periods.

In a different set of experiments, to determine whether these signals from V1 and RSPp to HVAs were composed of prediction errors, we compared GC structure of the NE group with the ME group during the mismatch periods in the SCL-VR (Fig. 4). The GC magnitude from V1 and RSPp to HVAs and other areas were large in the mismatch-unexperienced NE group (Fig. 6d), which is consistent with the result of the random mismatch experiment (Fig. 6c). However, in the ME group, the GC magnitude from V1 and RSPp to HVAs was small or not statistically significant

compared with the NE group. These results suggest that V1 and RSPp send the prediction error signals to multiple cortical areas, including HVAs and anterior areas.

Next, we investigated the anatomical circuit structure that underlies this signal flow in the mouse brain. Analysis of anterograde tracing data with AAV injections demonstrated the circuit organization from V1 to PM and AM as well as from RSPp to PM and AM (Supplementary Fig. 9). By retrograde tracing with RVΔG, we found that RSPp received inputs primarily from sensory and memory-related areas, such as the visual areas and hippocampal areas, whereas RSPa received inputs from motor and execution-related areas, such as the anterior cingulate area and secondary motor cortex (Supplementary Fig. 3). The difference in the responses and cortico–cortical communication profiles along the anterior–posterior axis in RSP during visuomotor mismatch events can be attributed to the difference in the circuit structure. Taken together, the information flow mediated via subnetworks in the posterior cortical areas support the notion of the hierarchical processing of prediction errors.

Discussion

The predictive coding hypothesis postulates hierarchical cortical communications for propagating prediction errors during visual perception, when inferring the cause of a change in sensory input from context [3,4,35]. Here, using wide-field calcium imaging from mice with pan-excitatory neuron expression of jGCaMP7f via AAV-PHP.eB injections, we found that posterior cortical areas PM, AM, and RSPp, in addition to V1, significantly responded to visuomotor mismatches between visual flow feedback and mouse movement. GC analysis revealed information flow from the V1 to HVAs during mismatch periods in contrast to during closed-loop periods, indicating hierarchical propagation of prediction errors (Fig. 2 and 6). Predictability of the visuomotor mismatch based on prior experiences significantly affected neural responses and the information flow in the posterior medial areas (V1, RSPp, PM, and AM) (Fig. 4 and 5). Thus, we conclude that prediction error signals were hierarchically encoded and propagated across posterior cortical areas.

Visual information is hierarchically processed across multiple cortical areas in the mammalian cortex [8,9,39,40]. Functional and anatomical properties differ between areas, suggesting ventral (LM, LI, POR) and dorsal (PM, AM, RL, AL, A) visual information processing streams [10,11]. Moreover, in primates, physiological and anatomical investigations indicate the existence of multiple substreams in dorsal visual pathway forming two distinct functional roles: the dorso–dorsal stream and the ventro–dorsal stream [41,42]. The present study demonstrated that PM and AM significantly differed from RL, AL, and A in the visuomotor mismatch responses, suggesting the presence of functionally segregated subnetworks within the dorsal stream of the mouse visual system. Therefore, prediction error signals can be processed along the dorso–dorsal stream in mice.

We demonstrated that the neural responses to the visuomotor mismatches were larger in the mismatch-unexperienced subjects than those in mismatch-experienced subjects (Fig. 4 and 5). A previous study argued that the “mismatch” response can simply be explained by visual and

locomotion-related modulation, without prediction error components [43]. In the SCL-VR, the locomotion speed and visual flow speed were almost equal at the mismatch onset timing on average between the NE and ME groups, because the mismatch timing was triggered by the predetermined locomotion speed of animals (Fig. 4A and 4D). Hence, the difference in the neural and behavioral responses between NE and ME mice is attributable to the difference in the presence or absence of prediction errors to the visuomotor mismatch events in the mice (Fig. 4c). Thus, we conclude that the smaller neural responses to the mismatches in ME mice than those in NE mice should result from smaller prediction errors due to learning from prior experiences for the visual flow mismatches in ME mice. In addition, accumulating evidence shows that the pupil size of animals is an indicator not only of light levels in the environment but also of internal states, such as arousal and surprise [17,44,45]. Therefore, the larger pupil response to the mismatch in NE mice than that in ME mice may reflect a prediction error component in the mismatch responses in NE mice. The observed decrease in the neural and pupil response magnitude after the subsequent experiences for the NE group also supports this interpretation (Fig. 5). Attinger *et al*. also demonstrated smaller behavioral and V1 responses to visuomotor mismatches in non-coupled visuomotor experienced mice than in normally coupled experienced mice, suggesting that the visuomotor mismatch responses were shaped by visual and motor coupled experiences during the development [31]. Taken together, the mismatch responses that we observed in the present study should be driven by prediction error components computed by comparisons between bottom-up sensory inputs and top-down predictions for the VR environment.

The RSP integrates inputs from multiple higher areas, including frontal cortical areas, sensory cortical areas, and hippocampal formations[46–49]. In addition, the RSP is a major source of V1[17] and provides the V1 with top-down information for visually guided action in an experience-dependent manner[50]. Notably, several distinct differences were identified in the visuomotor

mismatch response and input-output connectivity along the anterior–posterior axis of the RSP. The GC analysis suggests that RSPp sends a strong signal to visual areas and RSPa, particularly during visuomotor mismatch periods in the mismatch-unexperienced groups (Fig. 6). Anatomical investigations revealed that RSPp, along with visual areas and hippocampal areas, organized a visual and memory-related subnetwork, whereas RSPa, along with anterior cingulate areas, somatosensory areas, M1 and M2, organized a motor and execution-related subnetwork (Supplementary Fig. 3). Thus, rapid mismatch responses in RSPp could result from the comparison of egocentric spatial information provided by hippocampal areas to visual information provided by the V1. This idea is consistent with the previous studies showing that RSP neurons process context-dependent flexible behavior during visually guided navigation [27,28,51]. In future experiments, it will be important to test this possibility by projection-specific recording and manipulation in the RSPa and RSPp. Taken together, analyzing the functional architecture of the RSP should facilitate further understanding of context, action, and prediction coding in the brain.

Detecting unexpected visual inputs is critical for visually guided motor control, learning, and navigation. Accumulating evidence in primates and rodents suggests that visuomotor error signals in motor cortices drive adaptive motor learning[52,53]. A recently study demonstrated that the PM and AM are crucial for adaptation to abnormal visual feedback in VR environments [54]. We also found that the PM and AM have more axonal output to the frontal cortex than the V1 (Supplementary Fig. 9). Therefore, we speculate that the PM and AM send visuomotor error signals to the motor cortices. Future studies could test this model by manipulation of a projection-specific population [24,55,56]. Furthermore, electrophysiological recordings in previous work demonstrated that response properties to mismatches were different between layer 2/3 and layer 5 of the V1 [18]. From the immunohistochemistry for the mice infected with AAV-PHP.eB expressing jGCaMP7f under the CaMKII promotor, we speculate that the signals detected in this study were

derived from excitatory neurons on both superficial and deeper layers [56]. Therefore, to understand local circuit mechanisms computing prediction errors in HVAs, future studies should clarify the details of response characteristics at a single-cell resolution focusing on excitatory neuron subtypes.

Conclusively, we demonstrated sequential propagation of visuomotor prediction error signals from hierarchically lower visual areas to HVAs along the dorsal stream subnetworks of posterior cortical areas. This study provides experimental evidence of the cortico–cortical hierarchical organization underlying predictive processing in the brain, which will help to connect the theoretical and biological understanding of multimodal integration in sensory perception.

Methods

Animals

All animal procedures followed institutional and national guidelines and were approved by the Animal Care and Use Committee of Nagoya University. All efforts were made to reduce the number of animals used and minimize the suffering and pain of the animals. C57BL/6J mice were purchased from Nihon SLC. These animals were maintained in a temperature-controlled room (24 °C ± 1 °C) under a 12 h light/dark cycle with *ad libitum* access to food and water. Due to the body size needed for adaptation in head-fixed VR, mice aged 11−28 weeks were used in the VR experiments. All animals were reared in the normal light-dark cycle for evaluating the effect of the experiences in the VR. See Supplementary Table. 2 for the usage of each group of animals.

AAV production

The jGCaMP7f fragment was generated using PCR with PrimeSTAR Max DNA Polymerase (TaKaRa, Shiga, Japan) on a PCR thermal cycler (TP350, TaKaRa)[57,58]. The plasmids were digested with appropriate restriction enzymes (New England BioLabs, Ipswich, MA, USA) under optimal conditions. The digested plasmid and the PCR product were then assembled with NEBuilder HiFi DNA Assembly Master Mix (New England BioLabs). Chemically competent Stbl3 *Escherichia coli* cells (Thermo Fisher Scientific, Waltham, MA, USA) were transformed with the AAV plasmids. The plasmids were confirmed by diagnostic digestion with appropriate restriction enzymes and sequenced before virus production. AAVs were generated in HEK293T cells and purified with ultracentrifugation as previously described [22,59]. The genome titers of the AAVs were quantified by qPCR for the WPRE sequence. The titers of AAV-PHP.eB-CaMKII-jGCaMP7f and AAV-PHP.eB-hSyn-GFP were 3.25×10^{13} vg/mL and 2.96×10^{13} vg/ml, respectively. Virus aliquots were stored at −80 °C until use.

G-deleted rabies virus production

RVΔG-GFP[60] was recovered by transfection of B7GG cells with the rabies viral genome pSAD-B19ΔG-GFP vector, pcDNA-SAD-B19N, pcDNA-SAD-B19P, pcDNA-SAD-B19L, and pcDNA-SAD-B19G, and was maintained in a humidified atmosphere of 3% CO_2 at 35 °C. For *in vivo* injection, RVΔG-GFP was amplified in ten 15-cm dishes in a humidified atmosphere of 3% CO_2 at 35 °C, filtrated with a 0.45-μm filter, and concentrated by two rounds of ultracentrifugation. RVΔG-GFP was titrated with HEK-293T cells. The titer of RVΔG-GFP was $1.0 - 1.2 \times 10^9$ infectious units/mL.

Retro-orbital virus injection and surgery

After deep anesthesia with a mixture of medetomidine hydrochloride (0.75 mg/kg, Nihon Zenyaku, Fukushima, Japan), midazolam (4 mg/kg, Sandoz, Bayern, Germany), and butorphanol tartrate (5 mg/kg, Meiji Seika, Tokyo, Japan), 100 μl of AAV-PHP.eB vector was intravenously injected into the retro-orbital sinus of mice using a 30-gage needle (Becton Dickinson, Franklin Lakes, NJ, USA). The skin and membrane tissue on the skull were carefully removed, and the surface of the skull was covered with clear dental cement (204610402CL, Sun Medical, Shiga, Japan) 14−20 days after virus injection. We then implanted a custom-made metal head-plate to the skull for stable head fixation. We confirmed the visibility of jGCaMP7f- or GFP-derived green fluorescence under a fluorescent macroscope (M165FC, Leica, Hessen, Germany). During surgery, the eyes were covered with ointment (0.3% Ofloxacin, Toa) to prevent dry eye and unexpected injuries. After the surgery, atipamezole hydrochloride solution (0.75 mg/kg, Meiji Seika) was intraperitoneally injected into mice for rapid recovery from the effect of medetomidine hydrochloride.

Virus injection for retrograde tracing with RVΔG

Mice aged 8-weeks were anesthetized with the same procedure as that for retro-orbital injection. Mice were head-fixed on a stereotaxis apparatus (David Kopf Instruments). RVΔG-GFP (400 nl for each location) was injected into RSPa (AP: −1.5 mm, ML: 0.2–0.3 mm, depth: 0.3 and 0.6 mm from bregma) or RSPp (AP: −3.0 mm, ML: −0.5 mm, depth: 0.5 and 1.0 mm from bregma) at 100 nl/min with pulsed air pressure using a PICOSPRITZER III (Parker).

Immunostaining

The mice were anesthetized with intraperitoneal injection of a sodium pentobarbital solution (9.72 mg/kg, Nacalai, 26427-72). The mice were transcardially perfused with 50 mL of PBS followed by the same volume of 4% paraformaldehyde (PFA, Nacalai) in PBS. Brains were post-fixed with 4% PFA in PBS, 15% sucrose in PBS overnight, and then with 30% sucrose in PBS. The brains were subjected to histological analysis [57,60] Cryoprotected samples were sectioned at a thickness of 40 µm on a freezing microtome (REM-710, Yamato Kohki). The sections were rinsed with PBS, blocked for 1−2 h in a blocking solution (50% Blocking One (Nacalai, 03953-95) in 0.1% Triton X-100/PBS (PBST)), and then incubated overnight at 4°C with primary antibodies: rabbit anti-GFP (1:3000, Abcam, cat# ab6556), chicken anti-GFP (1:2000, Abcam, cat# ab13970), goat anti-PV (1:500, Swant, cat# PVG-213), rat anti-SOM (1:500, Millipore, cat# MAB354), and rabbit anti-VIP (1:400, ImmunoStar, cat# 20077) in 5% Blocking One/0.1% PBST. After three washes with 0.01% PBST, the sections were incubated with Alexa Fluor 488- or Alexa Fluor 594-labeled anti-mouse IgG, anti-rabbit IgG, anti-rat IgG, or anti-chicken IgY antibodies (1:1000, Jackson) and DAPI (Nacalai, 1.25 µg/ml).

We acquired images using a laser scanning confocal microscope (Zeiss, LSM800) with Plan Apo x10 (Zeiss, NA 0.45) or Plan Apo x20 (Zeiss, NA 0.75) objective lens. The specificity of the primary antibodies was confirmed by typical staining patterns. None of the observed labeling was due to nonspecific binding of secondary antibodies or autofluorescence in the fixed tissue because sections treated with secondary antibodies alone had no detectable signals. The acquired images were processed using ImageJ/Fiji for visualization.

Wide-field calcium imaging procedure

We monitored fluorescent signals with a customized macroscope (THT, Brainvision) based on a tandem lens design (a pair of Plan Apo 1x, WD = 61.5 mm, Leica) and epi-illumination system (see Supplementary Fig. 1). We used the alternating excitation method to filter the calcium-independent fluctuation from the calcium signal. The excitation light was provided by alternating blue (M470L4, Thorlabs) and violet (M405L3, Thorlabs) LEDs and filtered by additional band-pass filters (Blue: #86-352, Edmund; Violet: FBH400-40, Thorlabs). The excitation light was spatially equalized in the imaging area by a glass diffusion filter (DGUV10-600, Thorlabs). The average excitation LED power delivered to the surface was <5.0 mW. Fluorescent light was passed through a dichroic mirror (FF495-Di03, Semrock) and a combination of long-pass and short-pass filters (FEL0500 and FESH0650, Thorlabs) to the sCMOS camera (ORCA-Fusion, Hamamatsu Photonics). The timing of the excitation light was controlled by the global exposure timing signal of the camera. The timing signal to switch the LED was processed by an FPGA-based logic circuit (Analog Discovery 2, Digilent) and binary-counter IC (TC4520BP, Toshiba) in real-time. The timing and power of the light source were monitored by a high-sensitive photodetector (PDA10A2, Thorlabs).

We used HCImage Live (Hamamatsu Photonics) to record fluorescent images. In the timelapse recording, images were taken at 576 × 576 pixels resolution (4 pixels binning). Single-shot high-resolution images (2304 × 2304 pixels resolution) were also acquired to identify the anatomical landmarks finely at the end of the imaging session. The sampling rate of each wavelength image was 20.0 Hz, and practical exposure time (the duration of LED illumination per single frame) was 13.5 ms. The field of view was blocked from the light of the VR monitor by custom-designed 3D-printed poly-lactic acid parts painted with matt black lacquer composition to prevent the contamination of the fluorescent signal and visual stimuli. All imaging sessions were shorter than 2.5 h. We covered the surface of the coated skull with a silicone material after the imaging session to maintain the visibility of fluorescence. Only mice that showed regular locomotion on the treadmill were tested in further experiments.

Processing of imaging data

The acquired images were then compressed to a resolution of 288 × 288 pixels, and then motion correction was performed using the 405-nm excited images using efficient subpixel image registration algorithms [61]. A single template image for registration was used for the motion correction procedure in each imaging session. The signal of each pixel was processed by the linear regression method [24,25]. The 405-nm channel was resampled at 40.0 Hz using the interpolation method and then interpolated values were used for signal correction of the 470-nm channel. The processed signal was then smoothed using a moving average filter (width: 50 ms). Thereafter, all frames were registered to the top-view image of ACCF (330 × 285 pixels, corresponding to 13.2 × 11.4 mm in the ACCF) using two anatomical landmarks along the midline (the center of the olfactory bulb and base of the RSP) according to the previous study [62] with some modifications (Fig. 1). A scale bar is absent in registered images owing to image transformation from raw

recorded image. The registration to the ACCF for every mouse was confirmed based on both the resting-state connectivity map and retinotopic map (Fig. 1 and Supplementary Fig. 4b). A two-dimensional Gaussian filter was applied for pixel-based results presentation (sigma = 2 pixels).

To quantify the change in dF/F of the mismatch, visual feedback, and locomotion onset events, we defined the baseline frame for each event trial. The baseline frame of each trial was the average of the frames during 0.50 s for random mismatch (Fig. 2 and S6), and 0.25 s for semi-closed-loop VR (Fig. 4) before event onset. Since visual flow speed and the texture of walls were symmetric, the images or dF/Fs of the left and right hemispheres were computed independently, then data of the same trials were averaged (the image of the left hemisphere were mirrored) in all experiments except for pixel-based correlation analysis (Supplementary Fig. 6b and Supplementary Fig. 8). In the ROI-based analysis, the size of the ROI is 4 × 4 pixels. The maps of p-values (Fig. 3 and 4) were calculated with one-side Mann–Whitney U test for evaluating response statistical significance.

We evaluated the statistical significance with a bootstrap test to compare the set of different groups or sessions. In the analysis of the NE vs ME group (Fig. 4), we resampled the trial data from each group with a bootstrap procedure and made two pseudo distribution of trial-averaged response. Then, we evaluated the *p*-value by computing the overlap ratio of X/N, where X indicates overlapping samples between the two distributions, and N indicates iteration (1000 times resampling performed). In the analysis of the different session for same animals (Fig. 5e; NE group, Rec.1 vs Rec.2), a pseudo distribution was made by the subtraction of data recorded from same animal between Rec.1 and Rec.2, then the radio of trials below or above 0 in the distribution was quantified as the *p*-value. Results of the one-sided test for each timepoint and ROIs were presented in figures (Fig. 4i−j and 5e).

Virtual reality environment

The VR environment used in this study was adapted from the design described by Saleem and colleagues[63]. Mice were head-fixed and free to run on a one-dimensional treadmill. We used three frameless 3/4" monitors (LP097QX1, LG) equipped with anti-reflective film (TB-A18MFLKB, ELECOM) for visual stimulation and a 120 mm diameter urethane sponge for the treadmill stage. The rendering for these monitors was synchronized with a "Mosaic" function provided by the graphics card (Quadro P4000, NVIDIA). The speed of the subject's locomotion was monitored by the rotary encoder (360 pulses/cycle) connected to the microcontroller (Arduino Uno, Arduino CC). The time-series data of running speed were smoothed by Savitzky−Golay filter in the offline analysis (order = 3, frame length = 21). Visual feedback was provided by custom-written software in MATLAB (MATLAB 2020a, Mathworks). The latency of visual feedback is typically lower than 50 ms (corresponding to < 3 frames). The timing trigger of mismatch events was sent by the data acquisition board on the master PC (USB-6343, National Instruments) and received by the data acquisition board on the stimulus PC (USB-6002, National Instruments).

We constructed a virtual environment simulating an infinite corridor with blurred random dot patterns. The patterns on the left and right walls were completely symmetrical, with no distinct landmarks in the virtual environment. Visual flow stimuli (Supplementary Fig. 2) were presented within the same VR environment. Flow speed corresponded to 31 cm/s locomotion for the 1.5 sec/trial. The signal of the rotary encoder speed, LED power, exposure timing, and mismatch or forced visual flow timing were recorded by the data acquisition interface of the master PC with a custom-written MATLAB application at a 20 kHz sampling rate. The eye position, pupil size, and face of the mice were monitored by a machine vision camera equipped with an array of 940 nm wavelength IR-LEDs (AE-LED56V2, Akiduki-deshi), and a triacetate long-pass filter (cutoff wavelength = 820 nm, IR-82, Fujifilm). The demonstration movie of behaving mice

(Supplementary Movie 2) was recorded with a CMOS camera (iPhone 8, Apple). During the training and imaging sessions, the room light was off.

In the closed-loop VR (Fig. 2 and 6), mismatches were triggered by a random timing generator program on the master PC. Five mice were habituated under the head-fixed VR condition in 1−2 hour sessions for 3−5 days, until they showed regular locomotion in the VR setup (5.4, 4.0, 7.3, 7.0, 6.3 hours, respectively). Each imaging session had a habituation period of 15−30 min in the closed-loop VR before recording. For smooth head fixation, light anesthetization (1.0−1.5% Isoflurane) was adapted at a first habituation session.

In the semi-closed-loop VR (SCL-VR; Fig. 4, 5 and 6), mismatch events were triggered by mouse locomotion speed, computed by the stimulus PC in real-time. The mismatch was triggered when the locomotion speed exceeded the defined threshold (>6.0 cm/s, refractory period = 5.5s). The logic flow of visual feedback in the SCL-VR is represented in Fig. 4a. Six mice were habituated for 5 consecutive days (Fig. 4b); three mice were trained on the SCL-VR to experience visuomotor mismatches (ME group), and three mice were trained in the regular closed-loop VR as mismatch-unexperienced animals (NE group). NE groups were habituated for additional 4 days in the SCL-VR prior to second imaging session (Fig. 5b). The duration of habituation was 0.5 h for the first day and 1.5 h for days 2−5. On the first day, mice were habituated for head fixation on the treadmill in the dark for 30 min prior to the VR habituation (30 min).

Correlation map and GC analysis

To examine the information flow of the mismatch responses between cortical areas, we computed pairwise correlations between the activities of each ROI by Granger causality analysis using the multivariate GC toolbox. We adapted the pairwise conditional GC as the “GC.” When calculating the correlation map and GC magnitudes for closed-loop periods, neural signals before mismatch

onset (−1.5 to 0.0 s) were used for the analysis. To compute the correlation maps and the GC magnitudes for mismatch periods, neural signals during mismatch (0.0 to 1.5 s) were used for the analysis. The correlation coefficient was computed from the z-scored signal for each animal. The statistical significance of the correlation map was adapted using the z-statistic value for each pixel [64]. The time window of stationary or running in the dark was thresholded by the locomotion speed (running, >3.0 cm/s; stationary, <0.01 cm/s). The speed range between these two thresholds was excluded from the analysis for simplification.

Face video analysis

A single CMOS camera (DMX33UX174, The Imaging Source) was used to monitor animal movements. The camera was equipped to the basement of the VR system (MB3030D/M, Thorlabs) with a flexible arm to capture the face of the subject. We recorded face and eye movement videos of mice during each imaging session. The sampling rate of the video was around 20 Hz. All acquired frames were cropped to a resolution of 640 × 480 pixels^2 to reduce the cost of post-processing. To evaluate the effects of face and eye movement, we extracted the position of facial landmarks using DeepLabCut[65]. We defined the position of the eyelid (the edge of dorsal and ventral), pupil edge (edge of dorsal, ventral, anterior posterior), and nose (Fig. 2b). We used the "resnet_50" configuration for training the dataset. The training dataset was composed of movies recorded in the imaging and training sessions. The error of extracting position was within ~3 pixels. Blinking was detected by the rate of change in the distance between the upper and lower eyelids. Changes of >25% of the distance during the mismatch periods were defined as a blinking trial. Grooming and irregular behaviors were manually detected by the experimenter (R.F.T.).

Dorsal cortex-wide imaging under the anesthetized condition

Following the training and imaging session in VR, functional mapping of cortical areas was performed after the recovery period (4−7 days) from head-plate implantation (see also Resting-state connectivity mapping and Retinotopic mapping, below). The mice were lightly anesthetized by isoflurane inhalation (1.0% to 1.5%) during the imaging session. Body temperatures were maintained via heating pad. As for the VR-imaging session, the face of the mice was recorded by a CMOS camera under infrared lighting to monitor the state of subject arousal. The sessions in which mice showed distinct body movements were manually identified and excluded from the analysis. The concentration of isoflurane was manually controlled according to body and facial movements as monitored by the facial camera. Visual stimuli were presented on the same display used for the VR setup, and the treadmill setup was replaced with a stage with a heating pad equipped on a laboratory scissor jack. Imaging under the anesthetized condition was performed before the VR training session for five mice (used in Fig. 2 and 6), or after all imaging sessions in VR were finished for six mice (Fig. 1e–g and 3).

Resting-state connectivity mapping

Resting-state cortical dynamics were recorded from mice lightly anesthetized by isoflurane inhalation (1.0% to 1.5%) in the absence of artificial sensory stimuli. Mice received retro-orbital injections of AAV-PHP.eB-CaMKII-jGCaMP7f. We computed the seed-based Pearson's correlation map for each ROI. R-squared values were used for visualization (Fig. 1).

Retinotopic mapping

We presented drifting checkerboard stimuli in four directions (0, 90, 180, and 270 degrees), for 5 or 15 s. Typically, we presented 30 (for T = 5 s) or 19 (for T = 15 s) cycles of the stimuli to mice.

The contrast of the checkerboard was flickered at 5.0 Hz. Acquired images were then processed by phase-encoding methods to visualize the retinotopic map of the cortex [66].

Connectivity analysis of the anatomical database

We used the Allen Mouse Brain Connectivity Atlas to quantify the anatomical relationship between ROIs defined in wide-field calcium imaging datasets. The Allen Mouse Brain Connectivity Atlas consists of high-resolution images of axonal projections labeled with AAV injections into various locations. For identifying RSPa and RSPp output, we used normalized projection volume for quantification of output strength. We merged the data of 36 experiments (RSPa-IDs: 100140949, 166458363, 516838033, 292172100, 272735744, 267661018, 177907082, 159097209, 526502961, 166271142, 182338356, 288264753, 100148142, 166269090, 159832064, 292124058, 267658040, 308721884, 184168193, 278179794, 591535205, 287601100, 166325321, 308027576; RSPp-IDs: 157711043, 298720191, 181860879, 538078619, 584895127, 298275548, 521264566, 592540591, 166054929, 272916915, 112424813, and 182467736). For ease of interpretation, experiments using the combination of Ai75 line and CAV2-cre virus vector were excluded from the analysis. We used the Allen Software Development Kit in the Google Colaboratory environment for this analysis.

For the cortico–cortical connection analysis (Supplementary Fig. 9), we applied a spline regression approach to the data and estimated the cortico–cortical output patterns from each ROI[67]. All experiments targeted to the right hemisphere were included in this analysis. Projection density maps were normalized and visualized on a log scale.

Data availability

All data used for analysis are available from the corresponding authors on reasonable request. The experimental setup (3D-CAD data, circuit diagrams, and scripts for the VR) will be available on GitHub.

References

1. Kawato, M., Hayakawa, H. & Inui, T. A forward-inverse optics model of reciprocal connections between visual cortical areas. *Network: Computation in Neural Systems* **4**, 415–422 (1993).

2. Wolpert, D. M., Ghahramani, Z. & Jordan, M. I. An internal model for sensorimotor integration. *Science* **269**, 1880–1882 (1995).

3. Rao, R. P. & Ballard, D. H. Predictive coding in the visual cortex: a functional interpretation of some extra-classical receptive-field effects. *Nat. Neurosci.* **2**, 79–87 (1999).

4. Keller, G. B. & Mrsic-Flogel, T. D. Predictive Processing: A Canonical Cortical Computation. *Neuron* **100**, 424–435 (2018).

5. Felleman, D. J. & Van Essen, D. C. Distributed hierarchical processing in the primate cerebral cortex. *Cereb. Cortex* **1**, 1–47 (1991).

6. Nassi, J. J. & Callaway, E. M. Parallel processing strategies of the primate visual system. *Nat. Rev. Neurosci.* **10**, 360–372 (2009).

7. Glickfeld, L. L., Andermann, M. L., Bonin, V. & Reid, R. C. Cortico-cortical projections in mouse visual cortex are functionally target specific. *Nat. Neurosci.* **16**, 219–226 (2013).

8. Andermann, M. L., Kerlin, A. M., Roumis, D. K., Glickfeld, L. L. & Reid, R. C. Functional specialization of mouse higher visual cortical areas. *Neuron* **72**, 1025–1039 (2011).

9. Marshel, J. H., Garrett, M. E., Nauhaus, I. & Callaway, E. M. Functional specialization of seven mouse visual cortical areas. *Neuron* **72**, 1040–1054 (2011).

10. Murakami, T., Matsui, T. & Ohki, K. Functional Segregation and Development of Mouse Higher Visual Areas. *J. Neurosci.* **37**, 9424–9437 (2017).

11. Wang, Q., Sporns, O. & Burkhalter, A. Network analysis of corticocortical connections reveals ventral and dorsal processing streams in mouse visual cortex. *J. Neurosci.* **32**, 4386–4399 (2012).

12. Glickfeld, L. L. & Olsen, S. R. Higher-Order Areas of the Mouse Visual Cortex. *Annu Rev Vis Sci* **3**, 251–273 (2017).

13. Keller, G. B., Bonhoeffer, T. & Hübener, M. Sensorimotor mismatch signals in primary visual cortex of the behaving mouse. *Neuron* **74**, 809–815 (2012).

14. Crapse, T. B. & Sommer, M. A. Corollary discharge across the animal kingdom. *Nat. Rev. Neurosci.* **9**, 587–600 (2008).

15. Niell, C. M. & Stryker, M. P. Modulation of visual responses by behavioral state in mouse visual cortex. *Neuron* **65**, 472–479 (2010).

16. Saleem, A. B., Ayaz, A., Jeffery, K. J., Harris, K. D. & Carandini, M. Integration of visual motion and locomotion in mouse visual cortex. *Nat. Neurosci.* **16**, 1864–1869 (2013).

17. Leinweber, M., Ward, D. R., Sobczak, J. M., Attinger, A. & Keller, G. B. A Sensorimotor Circuit in Mouse Cortex for Visual Flow Predictions. *Neuron* **95**, 1420–1432.e5 (2017).

18. Jordan, R. & Keller, G. B. Opposing Influence of Top-down and Bottom-up Input on Excitatory Layer 2/3 Neurons in Mouse Primary Visual Cortex. *Neuron* **108**, 1194-1206.e5 (2020).

19. Heindorf, M. & Keller, G. B. Reduction of layer 5 mediated long-range cortical communication by antipsychotic drugs. *bioRxiv* 2022.01.31.478462 (2022) doi:10.1101/2022.01.31.478462.

20. O'Toole, S. M., Oyibo, H. K. & Keller, G. B. Prediction error neurons in mouse cortex are molecularly targetable cell types. *bioRxiv* 2022.07.20.500837 (2022) doi:10.1101/2022.07.20.500837.

21. Dana, H. *et al.* High-performance calcium sensors for imaging activity in neuronal populations and microcompartments. *Nat. Methods* **16**, 649–657 (2019).

22. Chan, K. Y. *et al.* Engineered AAVs for efficient noninvasive gene delivery to the central and peripheral nervous systems. *Nat. Neurosci.* **20**, 1172–1179 (2017).

23. Lerner, T. N. *et al.* Intact-Brain Analyses Reveal Distinct Information Carried by SNc Dopamine Subcircuits. *Cell* **162**, 635–647 (2015).

24. Allen, W. E. *et al.* Global Representations of Goal-Directed Behavior in Distinct Cell Types of Mouse Neocortex. *Neuron* **94**, 891-907.e6 (2017).

25. Musall, S., Kaufman, M. T., Juavinett, A. L., Gluf, S. & Churchland, A. K. Single-trial neural dynamics are dominated by richly varied movements. *Nat. Neurosci.* **22**, 1677–1686 (2019).

26. Wang, Q. *et al.* The Allen Mouse Brain Common Coordinate Framework: A 3D Reference Atlas. *Cell* **181**, 936-953.e20 (2020).

27. Franco, L. M. & Goard, M. J. A distributed circuit for associating environmental context with motor choice in retrosplenial cortex. *Sci Adv* **7**, eabf9815 (2021).

28. Vann, S. D., Honey, R. C. & Aggleton, J. P. Lesions of the mammillothalamic tract impair the acquisition of spatial but not nonspatial contextual conditional discriminations. *Eur. J. Neurosci.* **18**, 2413–2416 (2003).

29. Makino, H. *et al.* Transformation of Cortex-wide Emergent Properties during Motor Learning. *Neuron* **94**, 880-890.e8 (2017).

30. Zmarz, P. & Keller, G. B. Mismatch Receptive Fields in Mouse Visual Cortex. *Neuron* **92**, 766–772 (2016).

31. Attinger, A., Wang, B. & Keller, G. B. Visuomotor Coupling Shapes the Functional Development of Mouse Visual Cortex. *Cell* **169**, 1291-1302.e14 (2017).

32. Abdolrahmani, M., Lyamzin, D. R., Aoki, R. & Benucci, A. Attention separates sensory and motor signals in the mouse visual cortex. *Cell Rep.* **36**, 109377 (2021).

33. Clancy, K. B., Orsolic, I. & Mrsic-Flogel, T. D. Locomotion-dependent remapping of distributed cortical networks. *Nat. Neurosci.* **22**, 778–786 (2019).

34. West, S. L. *et al.* Wide-Field Calcium Imaging of Dynamic Cortical Networks during Locomotion. *Cereb. Cortex* (2021) doi:10.1093/cercor/bhab373.

35. Friston, K. Hierarchical models in the brain. *PLoS Comput. Biol.* **4**, e1000211 (2008).

36. Pinto, L. *et al.* Task-Dependent Changes in the Large-Scale Dynamics and Necessity of Cortical Regions. *Neuron* **104**, 810-824.e9 (2019).

37. Barnett, L. & Seth, A. K. The MVGC multivariate Granger causality toolbox: a new approach to Granger-causal inference. *J. Neurosci. Methods* **223**, 50–68 (2014).

38. Kondo, M. & Matsuzaki, M. Neuronal representations of reward-predicting cues and outcome history with movement in the frontal cortex. *Cell Rep.* **34**, 108704 (2021).

39. Orban, G. A. Higher order visual processing in macaque extrastriate cortex. *Physiol. Rev.* **88**, 59–89 (2008).

40. Siegle, J. H. *et al.* Survey of spiking in the mouse visual system reveals functional hierarchy. *Nature* **592**, 86–92 (2021).

41. Rizzolatti, G. & Matelli, M. Two different streams form the dorsal visual system: anatomy and functions. *Exp. Brain Res.* **153**, 146–157 (2003).

42. Kravitz, D. J., Saleem, K. S., Baker, C. I. & Mishkin, M. A new neural framework for visuospatial processing. *Nat. Rev. Neurosci.* **12**, 217–230 (2011).

43. Muzzu, T. & Saleem, A. B. Feature selectivity can explain mismatch signals in mouse visual cortex. *Cell Rep.* **37**, 109772 (2021).

44. Reimer, J. *et al.* Pupil fluctuations track rapid changes in adrenergic and cholinergic activity in cortex. *Nat. Commun.* **7**, 13289 (2016).

45. Breton-Provencher, V. & Sur, M. Active control of arousal by a locus coeruleus GABAergic circuit. *Nat. Neurosci.* **22**, 218–228 (2019).

46. Cembrowski, M. S. *et al.* Dissociable Structural and Functional Hippocampal Outputs via Distinct Subiculum Cell Classes. *Cell* **173**, 1280-1292.e18 (2018).

47. Vann, S. D., Aggleton, J. P. & Maguire, E. A. What does the retrosplenial cortex do? *Nat. Rev. Neurosci.* **10**, 792–802 (2009).

48. Yamawaki, N., Corcoran, K. A., Guedea, A. L., Shepherd, G. M. G. & Radulovic, J. Differential Contributions of Glutamatergic Hippocampal→Retrosplenial Cortical Projections to the Formation and Persistence of Context Memories. *Cereb. Cortex* **29**, 2728–2736 (2019).

49. Yamawaki, N., Radulovic, J. & Shepherd, G. M. G. A Corticocortical Circuit Directly Links Retrosplenial Cortex to M2 in the Mouse. *J. Neurosci.* **36**, 9365–9374 (2016).

50. Makino, H. & Komiyama, T. Learning enhances the relative impact of top-down processing in the visual cortex. *Nat. Neurosci.* **18**, 1116–1122 (2015).

51. Campbell, M. G., Attinger, A., Ocko, S. A., Ganguli, S. & Giocomo, L. M. Distance-tuned neurons drive specialized path integration calculations in medial entorhinal cortex. *Cell Rep.* **36**, 109669 (2021).

52. Inoue, M., Uchimura, M. & Kitazawa, S. Error Signals in Motor Cortices Drive Adaptation in Reaching. *Neuron* **90**, 1114–1126 (2016).

53. Heindorf, M., Arber, S. & Keller, G. B. Mouse Motor Cortex Coordinates the Behavioral Response to Unpredicted Sensory Feedback. *Neuron* **99**, 1040-1054.e5 (2018).

54. Minderer, M., Brown, K. D. & Harvey, C. D. The Spatial Structure of Neural Encoding in Mouse Posterior Cortex during Navigation. *Neuron* **102**, 232-248.e11 (2019).

55. Waters, J. Sources of widefield fluorescence from the brain. *Elife* **9**, (2020).

56. Ren, C. & Komiyama, T. Characterizing Cortex-Wide Dynamics with Wide-Field Calcium Imaging. *J. Neurosci.* **41**, 4160–4168 (2021).

57. Okigawa, S. *et al.* Cell type- and layer-specific convergence in core and shell neurons of the dorsal lateral geniculate nucleus. *J. Comp. Neurol.* **529**, 2099–2124 (2021).

58. Suzuki, T., Morimoto, N., Akaike, A. & Osakada, F. Multiplex Neural Circuit Tracing With G-Deleted Rabies Viral Vectors. *Front. Neural Circuits* **13**, 77 (2019).

59. Konno, A. & Hirai, H. Efficient whole brain transduction by systemic infusion of minimally purified AAV-PHP.eB. *J. Neurosci. Methods* **346**, 108914 (2020).

60. Osakada, F. *et al.* New rabies virus variants for monitoring and manipulating activity and gene expression in defined neural circuits. *Neuron* **71**, 617–631 (2011).

61. Guizar-Sicairos, M., Thurman, S. T. & Fienup, J. R. Efficient subpixel image registration algorithms. *Opt. Lett.* **33**, 156–158 (2008).

62. Couto, J. *et al.* Chronic, cortex-wide imaging of specific cell populations during behavior. *Nat. Protoc.* **16**, 3241–3263 (2021).

63. Saleem, A. B., Diamanti, E. M., Fournier, J., Harris, K. D. & Carandini, M. Coherent encoding of subjective spatial position in visual cortex and hippocampus. *Nature* **562**, 124–127 (2018).

64. Cohen, J., Cohen, P., West, S. G. & Aiken, L. S. Applied multiple regression/correlation analysis for the behavioral sciences, 3rd ed. **3**, 703 (2003).

65. Mathis, A. *et al.* DeepLabCut: markerless pose estimation of user-defined body parts with deep learning. *Nat. Neurosci.* **21**, 1281–1289 (2018).

66. Kalatsky, V. A. & Stryker, M. P. New paradigm for optical imaging: temporally encoded maps of intrinsic signal. *Neuron* **38**, 529–545 (2003).

67. Knox, J. E. *et al.* High-resolution data-driven model of the mouse connectome. *Netw Neurosci* **3**, 217–236 (2019).

Acknowledgments

Competing interests: Authors declare that they have no competing interests.

Data and materials availability:

The datasets supporting this study and AAVs and RVs generated in this study are available from the corresponding authors upon reasonable request. All data needed to evaluate the conclusions in the paper are present in the paper and/or the Supplementary Materials. Additional data related to this paper will be provided upon reasonable request.

Figures

Fig.1

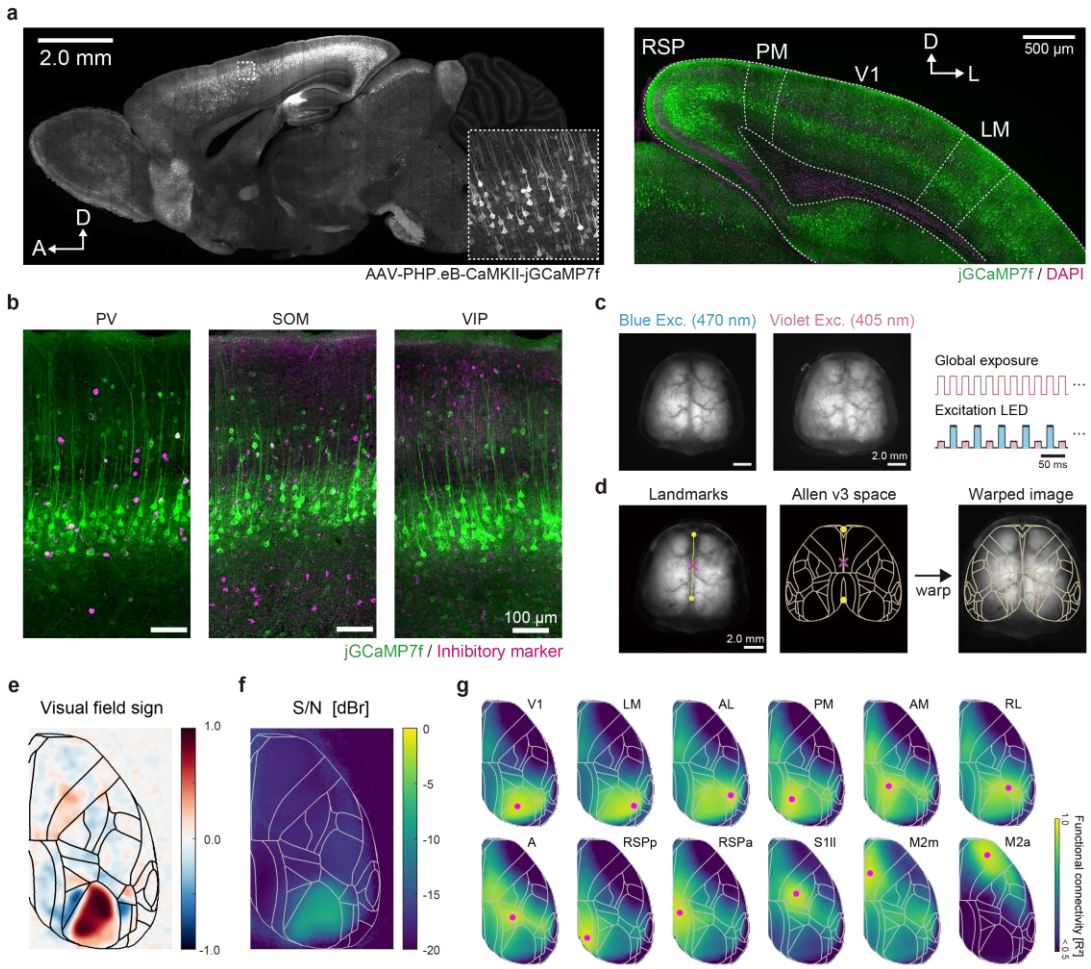

Fig. 1: Virus infection and wide-field Ca^{2+} imaging.

(a) Left: Fluorescent images of jGCaMP7f expression. Inset: individual neurons expressing jGCaMP7f. Right: A coronal image of the jGCaMP7f-expressing brain. Arrows indicate anterior (A), dorsal (D), and lateral (L) axes.

(b) Immunohistochemistry of inhibitory neuron subtype markers and jGCaMP7f.

(c) Schematics of dual-wavelength excitation switching. Left: Fluorescent images of the living brain illuminated by blue/violet excitation light sources. Right: Trigger timing and actual excitation timing.

(d) Registration process from the acquired brain image to the ACCF space. Left: Manually mapped landmarks on the pre-registration fluorescent image of living animal's brain (illuminated by 470 nm) and the areal border of ACCF. Right: The post registration image. Yellow dots indicate control points, center of olfactory bulb and base of retrosplenial cortex (RSP). Magenta crosses indicate the bregma.

(e) An averaged visual field sign map (n = 6 mice).

(f) A signal-to-noise ratio (S/N) map (n = 6 mice) during periodic moving checkerboard visual stimuli.

(g) Functional connectivity maps (n = 6 mice). Magenta dots indicate the center of ROI for the seed-based correlation map. Maps were computed by the average across the right and left hemispheres of each mouse. V1, primary visual area; LM, lateromedial visual area; AL, anterolateral visual area; PM, posteromedial visual area; AM, anteromedial visual area; RL, rostrolateral visual area; S1ll, primary somatosensory area, lower limb; RSPp, posterior part of RSP; RSPa, anterior part of RSP; M2m and M2a, medial and anterior part of secondary motor area, respectively.

Fig.2

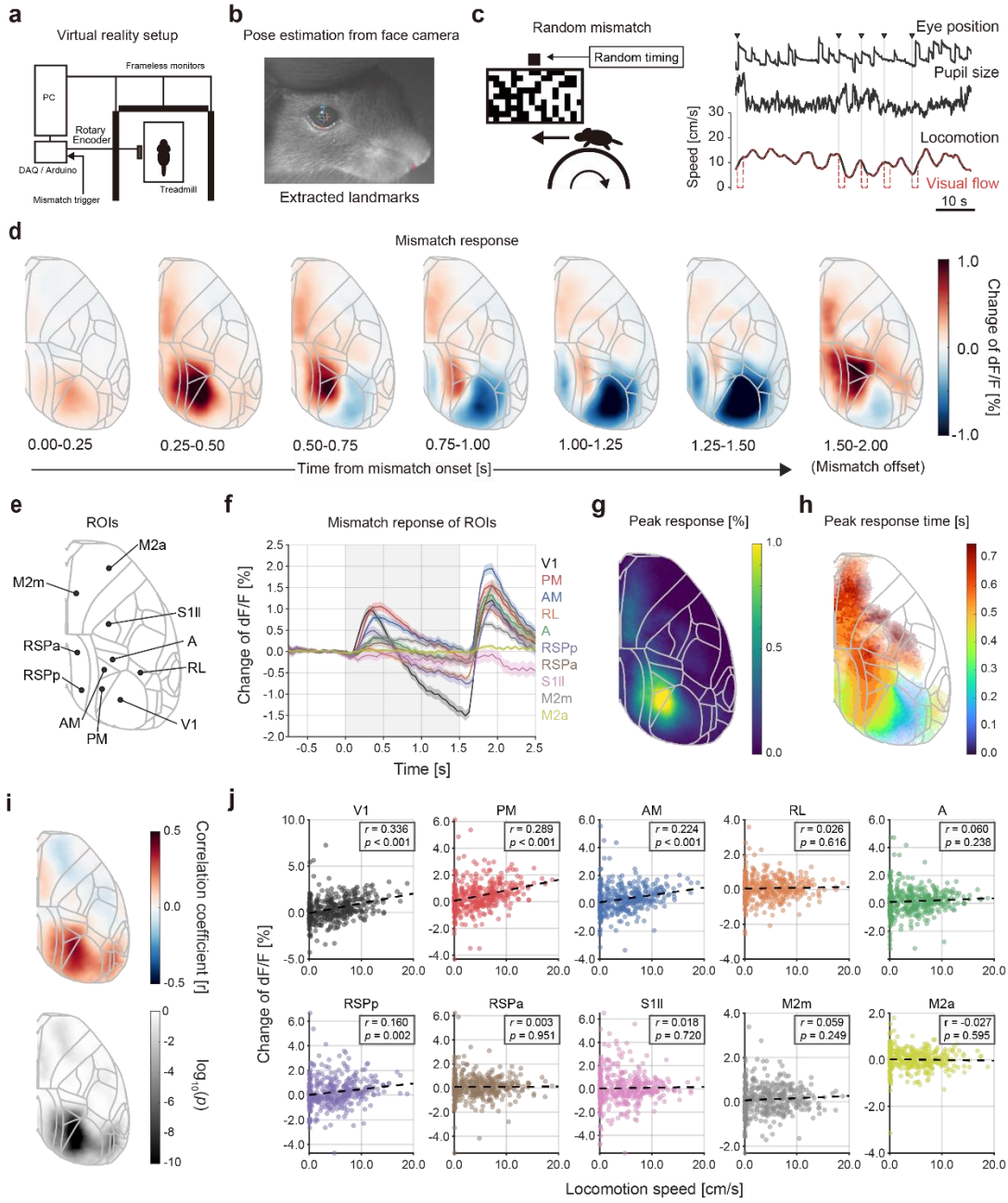

Fig. 2: Dorsal cortex-wide response to visuomotor mismatch.

(a) Schematic of virtual reality setup.

(b) An image of facial video data with extracted landmarks (cross marks).

(c) Left: Schematic of random timing feedback mismatch in the VR. Right: Example time process of mismatch and extracted behavioral parameters. Arrowheads indicate the timing of mismatch onset.

(d) Trial-averaged response to visuomotor mismatch event (253 trials from 5 mice).

(e) Locations of ten ROIs on the top view of the ACCF

(f) Averaged response traces from ten cortical areas. The shaded region indicates mismatch periods (0.0−1.5 s). Line traces represent means ± SEM.

(g) Response magnitude map during a mismatch period (0.0−1.5 s).

(h) Peak response time map during the mismatch period. Transparency was configured based on the response magnitude map.

(i) Linear correlation coefficient between locomotion speed of the mismatch onset (mean of −0.25−0.25 s) and neural response magnitude of all pixels in the ACCF. Pearson's correlation coefficient value (top) and p-value (bottom).

Fig.3

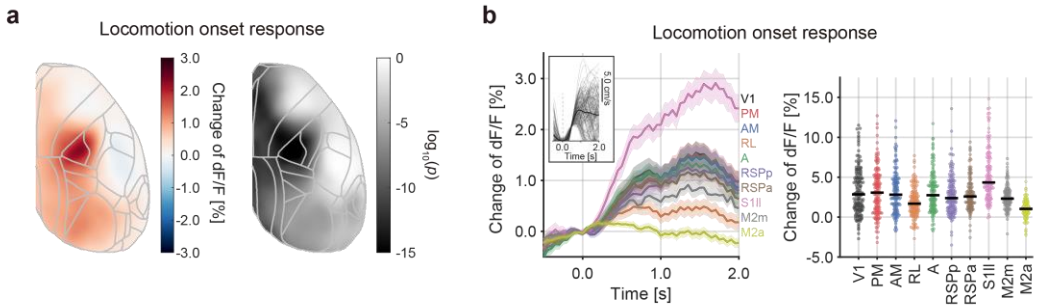

Fig. 3: Dorsal cortex-wide activity at the locomotion onset.

(a) Left: Locomotion onset response map (n = 5 mice). Right: Statistical significance of each pixel (one-tailed Signed−Rank test). Response traces from 10 cortical areas. Inset: Running speed of each trial. Bold black line indicates the trail average.

(b) Right: The distribution of response peak (time window 0.0−1.0 s from the onset), lines indicate the median.

Fig.4

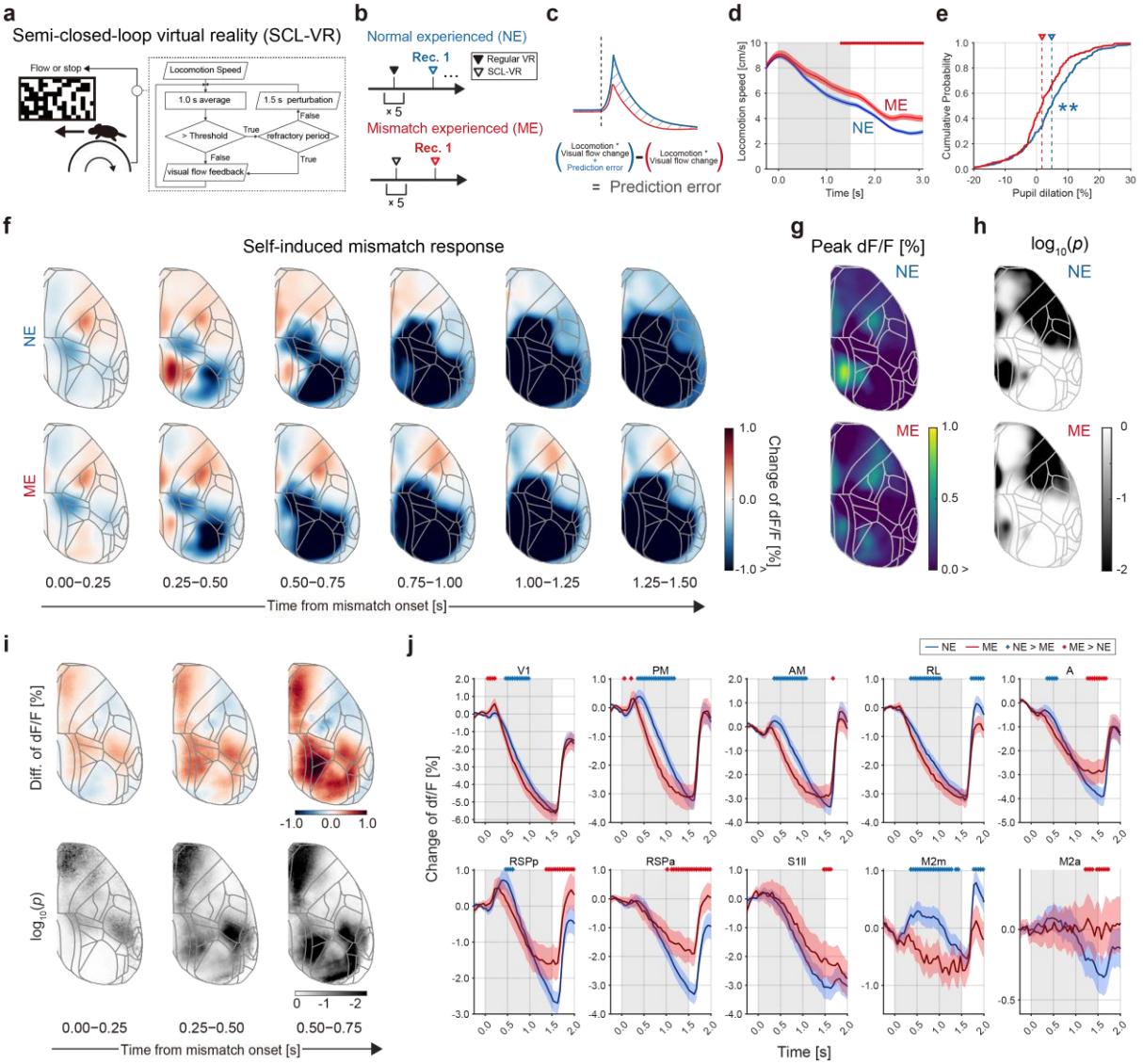

Fig. 4: Mismatch responses in the cortex depend on visuomotor experience history

(a) Schematic of semi-closed-loop virtual reality (SCL-VR), with inset showing the logic flow of visual feedback.

(b) Habituation history of two groups of animals (Normal experienced or Mismatch-experienced group). Normal experienced mice are naïve to mismatch events, whereas mismatch-experienced mice can predict the timing of mismatch events.

(c) The hypothetical neural response to mismatch event of the NE and ME animal. The prediction error of ideal ME animals is expected to decrease.

(d) Locomotion speed of mice during self-induced mismatch event. The shaded region indicates mismatch periods (0.0−1.5 s). Line traces represent means ± SEM. Dots show time bins with statistical significance ($p < 0.01$, one-tailed unpaired *t*-test).

(e) The cumulative distribution plot of pupil dilation response to the mismatch onset trials (0.0 to 1.0 s average). Dashed line indicates median value for each group. The asterisk shows statistical significance ($p < 0.01$, Mann–Whitney U test).

(f) Trial-averaged responses to during- and post-visuomotor mismatch events (NE: 268 trials from 3 mice; ME: 156 trials from 3 mice).

(g) Response peak magnitude map during a mismatch period (0.0−1.5 s).

(h) Statistical significance of response (average of [0.0 to 0.5 s] vs [−0.5 to 0.0 s], one-tailed Signed–Rank test).

(i) Top: The difference of response to self-induced mismatch response (NE–ME). Bottom: The statistical significance between NE and ME (one-tailed bootstrap test).

(j) Trial-averaged response traces from 10 cortical areas. The shaded region indicates mismatch periods (0.0−1.5 s). Blue plots indicate the data from NE animals. Red plots indicate the data from ME animals. Each plot is shown as a mean ± 95% confidence interval. Dots indicate time bins with statistical significance (bootstrap test, $p < 0.05$). Dot color indicates the alternative hypothesis (Blue: NE > ME; Red: ME > NE).

Fig.5

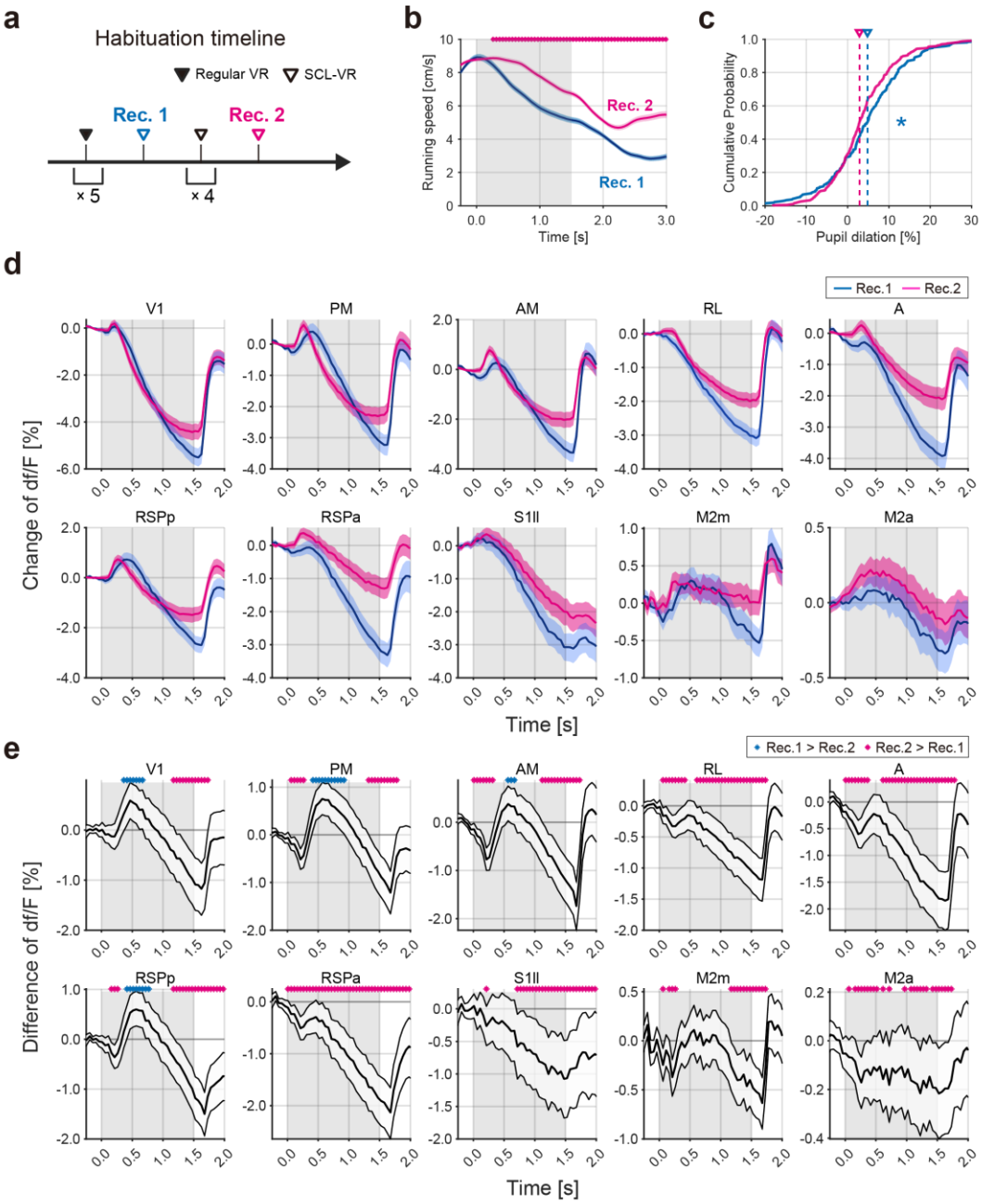

Fig. 5: Experience-dependent changes in the neural responses to visuomotor mismatch.

(a) Habituation history of subjects. Subjects (NE mice used in Fig.4) experienced additional four habituation sessions in the SCL-VR prior to the second recording session (Rec.2).

(b) Locomotion speed of mice during self-induced mismatch event. The shaded region indicates mismatch periods (0.0−1.5 s). Line traces represent means ± SEM (Blue: First recording session, Magenta: Second recording session). Dots show time bins with statistical significance ($p < 0.01$, one-tailed unpaired *t*-test).

(c) Cumulative distribution plot of pupil dilation response to the mismatch onset trials (0.0−1.0 s average). Dashed line indicates median value for each group. The asterisk shows statistical significance ($p < 0.05$, Mann–Whitney U test).

(d) Trial-averaged response traces from ten cortical areas. The shaded region indicates mismatch periods (0.0−1.5 s). Blue plots indicate data from the first recording session. Magenta plots indicate data from the second recording session. Each plot is shown as a mean ± 95% confidence interval.

(e) The difference of mismatch response between recording Rec. 1 and Rec. 2 (subtraction was applied between same animal's data). Each plot is shown as a mean ± 95% confidence interval. Dots indicates time bins with statistical significance (one-tailed bootstrap test, $p < 0.05$). Dot color indicates the alternative hypothesis (Blue: Rec. 1 > Rec. 2; Magenta: Rec. 2 > Rec. 1).

Fig.6

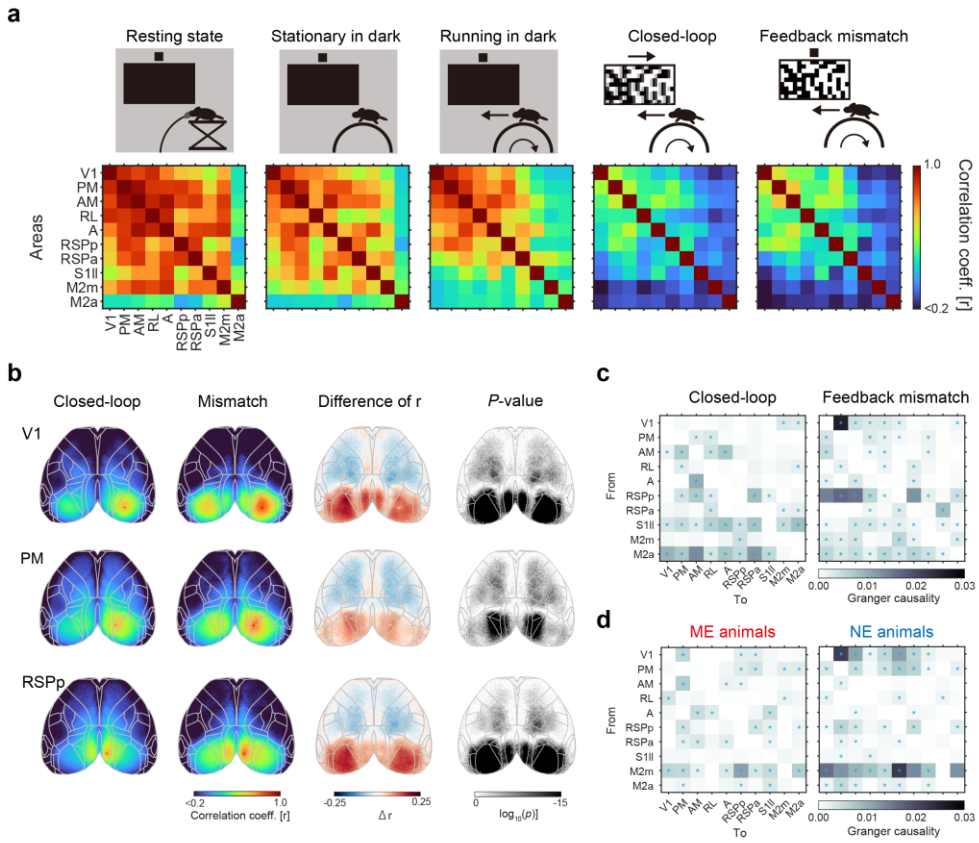

Fig. 6: Cortico–cortical communications under different contexts.

(a) Top: Schematic of five different behavioral and environmental contexts. Bottom: Pairwise linear correlation coefficient matrices between ten areas for different contexts (n = 5 mice).

(b) Seed-based correlation map of three areas (V1, PM, and RSPp) under the closed-loop and mismatch periods, and difference in the correlation coefficient and statistical significance (two-tailed z-statistics test) in (A).

(c) Matrix of the Granger causality of neural activity during closed-loop and mismatch periods (n = 253 trials from 5 mice).

(d) Matrix of the Granger causality of neural activity during self-induced mismatch periods of ME and NE animals (ME: n = 156 trials from 3 mice, NE: n = 268 trials from 3 mice).

Supplementary Information

Posteromedial cortical networks encode visuomotor prediction errors

Ryosuke F. Takeuchi,[1] Kei N. Ito,[1] Rumina Ueda,[1] Masahiro Yamaguchi,[1] Fumitaka Osakada[1,2,3,4,5]*

Contents

Supplementary Figure 1.

Supplementary Figure 2.

Supplementary Figure 3.

Supplementary Figure 4.

Supplementary Figure 5.

Supplementary Figure 6.

Supplementary Figure 7.

Supplementary Figure 8.

Supplementary Figure 9.

Supplementary Table 1.

Supplementary Table 2.

Supplementary Movie 1.

Supplementary Movie 2.

Supplementary Movie 3.

Supplementary Movie 4.

Supplementary Movie 5.

Supplementary Movie 6.

Fig.S1

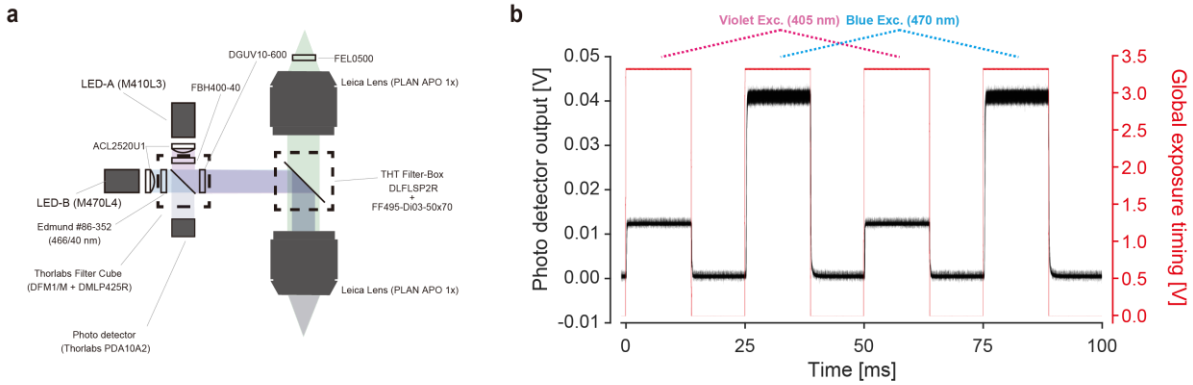

Supplementary Figure 1: Optical setup and control of LED flickering

(a) Schematic of the optical fluorescent imaging system.

(b) The latency of the global exposure strobe signal from the camera to the LED illumination.

Fig.S2

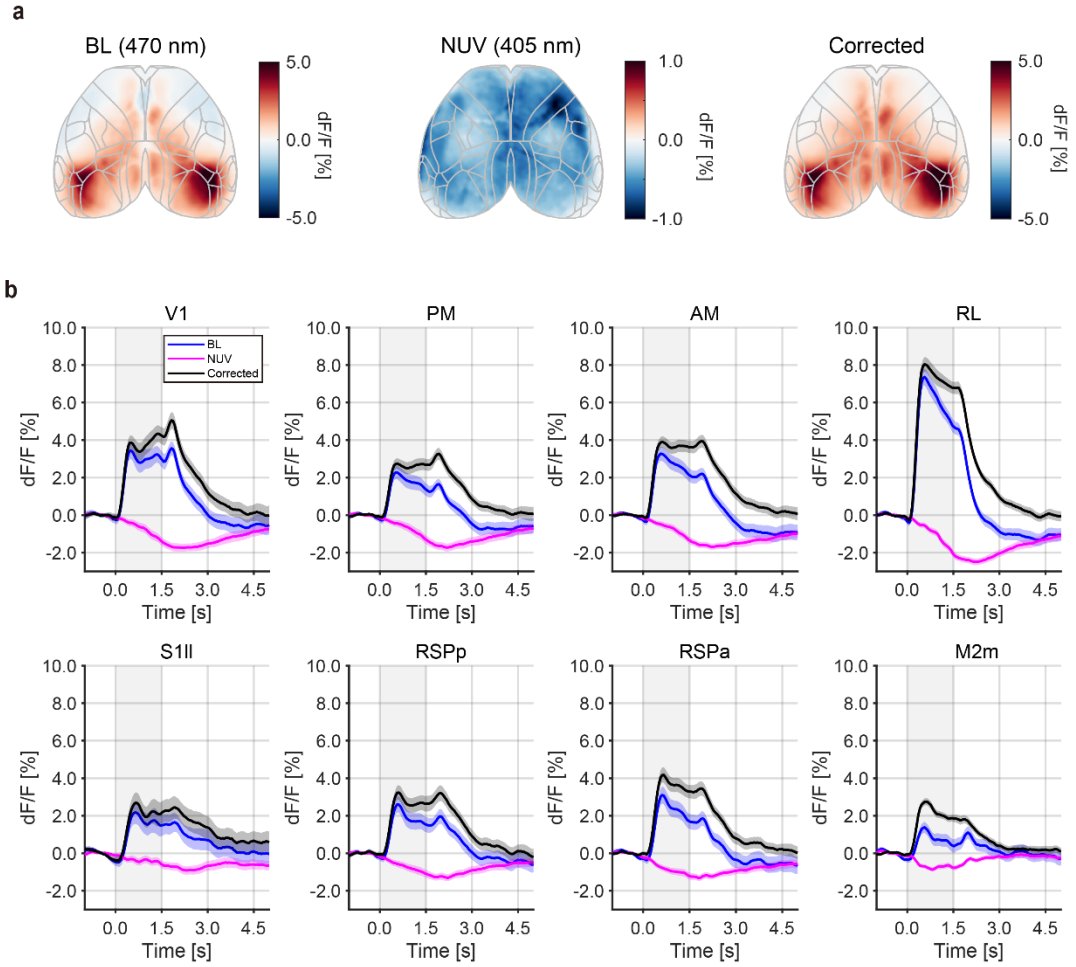

Supplementary Figure 2: Multi-wavelength switching effectively canceled intrinsic signals

(a) Neural response maps to brief visual flow onset. The maps were generated by averaging the flow onset periods (0.0−1.0 s).

(b) Neural response of eight brain areas. Gray shaded lines indicate visual flow periods.

Fig.S3

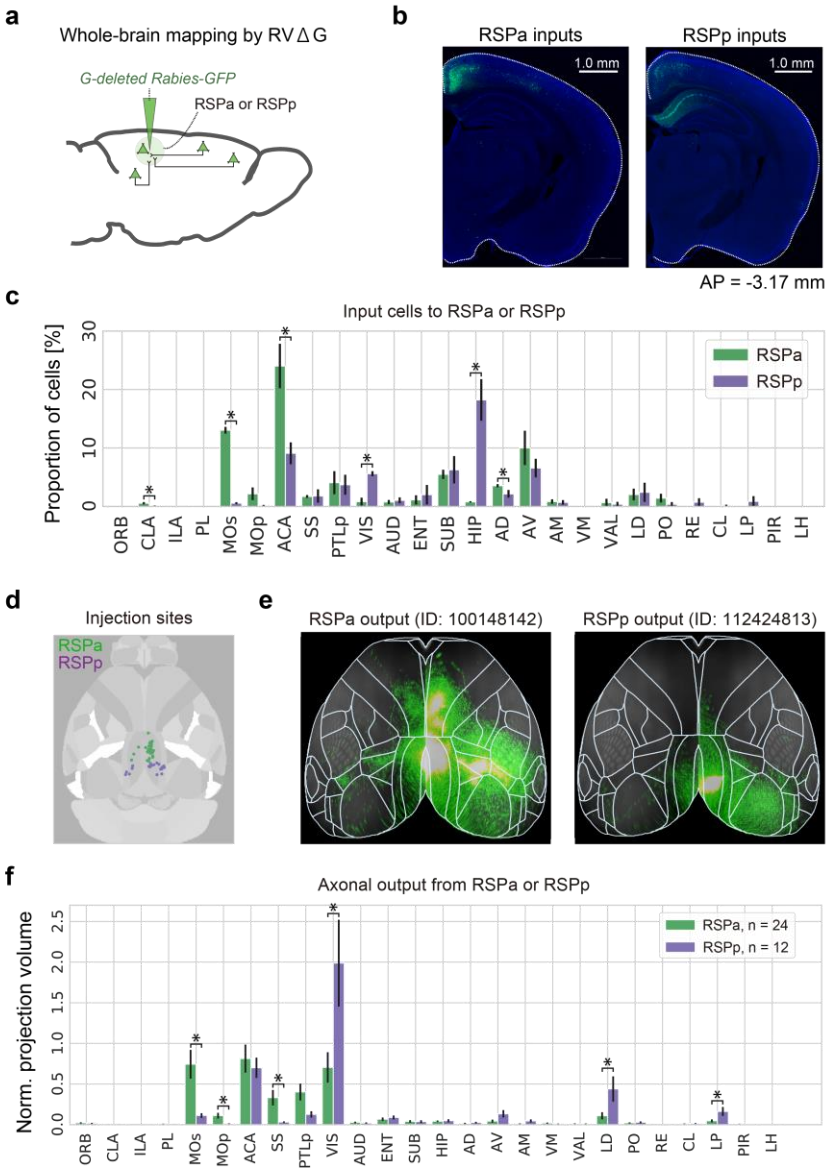

Supplementary Figure 3: Anatomical structure of RSPa and RSPp

(a) The schematic of retrograde tracing with RVΔG-GFP from RSPa or RSPp

(b) Example images of infected cells projecting to RSPa or RSPp. Coronal sections at 3.17-mm posterior to the bregma.

(c) Summary of inputs to RSPa or RSPp neurons. Asterisks show statistical significance (n = 3 mice, data are shown as means ± SEM, $p < 0.05$, Mann–Whitney U test)

(d) Injection sites of AAV for anterograde tracing. Data are from Allen mouse brain connectivity atlas.

(e) Top view of axonal cortical output of example injection experiments (adapted from Allen mouse brain connectivity atlas). Experiment IDs are indicated at the top.

(f) Summary of inputs to RSPa or RSPp neurons. Normalized projection volume was used for the quantification (means ± SEM). Asterisks show statistical significance ($p < 0.05$, Mann–Whitney U test).

Fig.S4

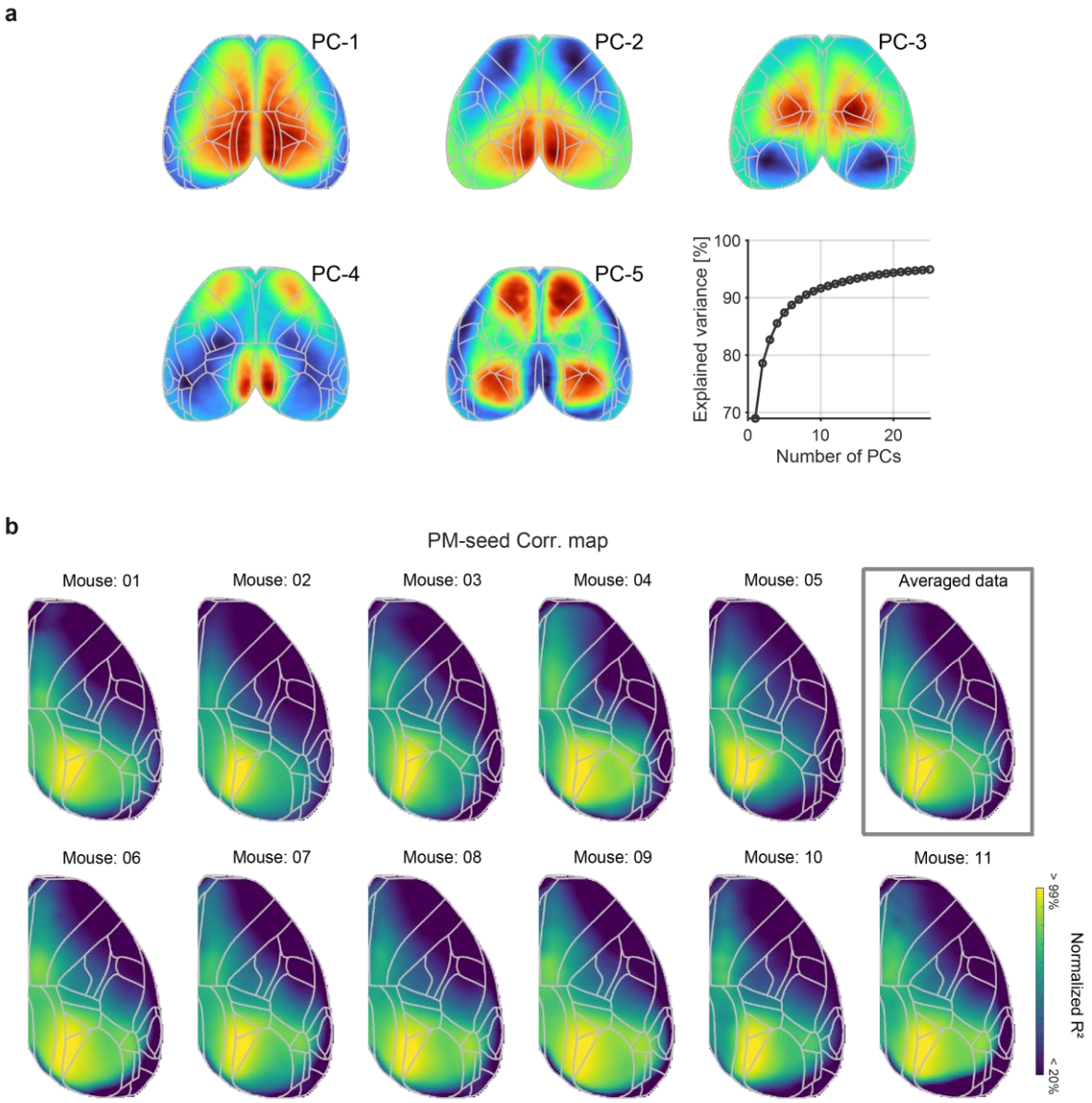

Supplementary Figure 4: Resting-state activity overlaid on Allen common coordinate framework

(a) Principal component analysis (PCA) of the resting-state cortical activity. Weight maps of PCA (1st −5th components) made from eleven mice. Right bottom: Cumulative explained variance by PCs.

(b) Functional connectivity maps of all animals (PM-seed, n = 11 mice). Maps are the average across the right and left hemispheres of each mouse.

Fig.S5

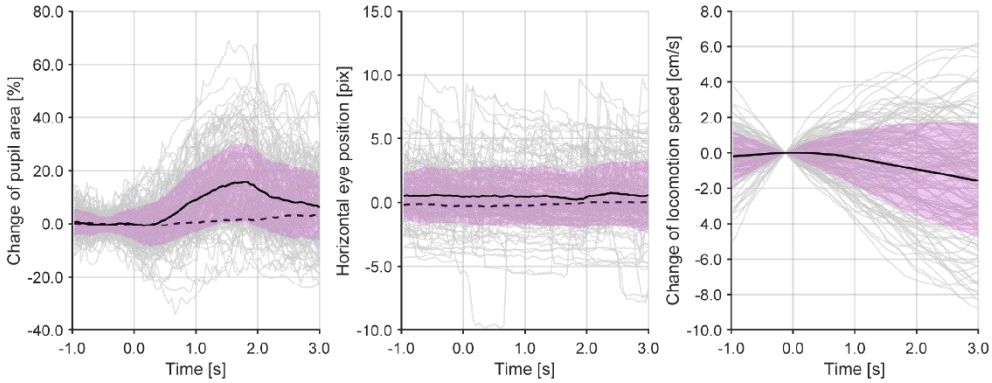

Supplementary Figure 5: Pupil area, eye position, and locomotion speed during mismatch periods

Left: pupil area dilation during mismatch periods (0.0−1.5 s). Middle: Horizontal eye position. Right: Changes in locomotion speed. Black lines indicate trial average, shaded magenta regions indicate S.D. Gray lines are the data of each trial. Dashed line indicates the trials in which the mouse's speed was slower than the threshold (3.0 cm/s).

Fig.S6

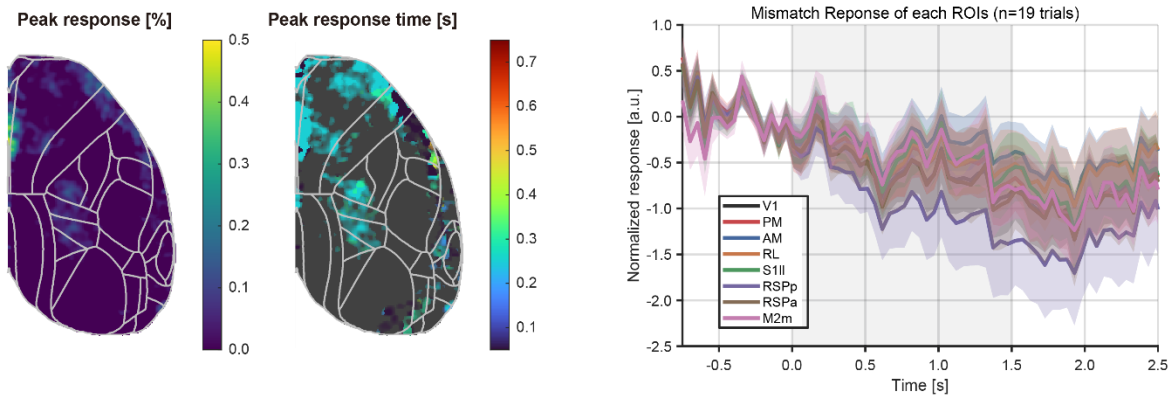

Supplementary Figure 6: Fluorescent change in the mouse expressing GFP by AAV-PHP.eB-hSyn-GFP

Left: Peak response amplitude map during mismatch periods (0.0−1.5 s from mismatch onset; related to Fig. 2G).

Middle: Peak response amplitude map during mismatch periods (0.0−1.5 s from mismatch onset; r related to Fig. 2H).

Right: The trace of mismatch response in ten ROIs. Shaded regions indicate SEM.

Fig.S7

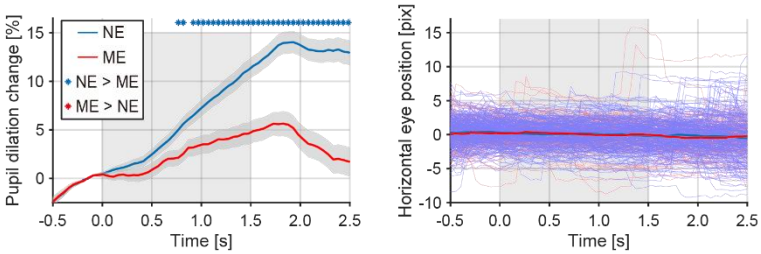

Supplementary Figure 7: Pupil response to visuomotor mismatch in semi closed-loop VR

Left: Pupil dilation change during self-induced visuomotor mismatch. Dots indicate the statistical significance between ME and NE mice (Blue: NE, Red: ME, one-tailed unpaired *t*-test, $p < 0.05$)

Right: Horizontal eye position change during self-induced visuomotor mismatch. Thin lines indicate each trial response, bold lines indicate trial averaged response (Blue: NE, Red: ME)

Fig.S8

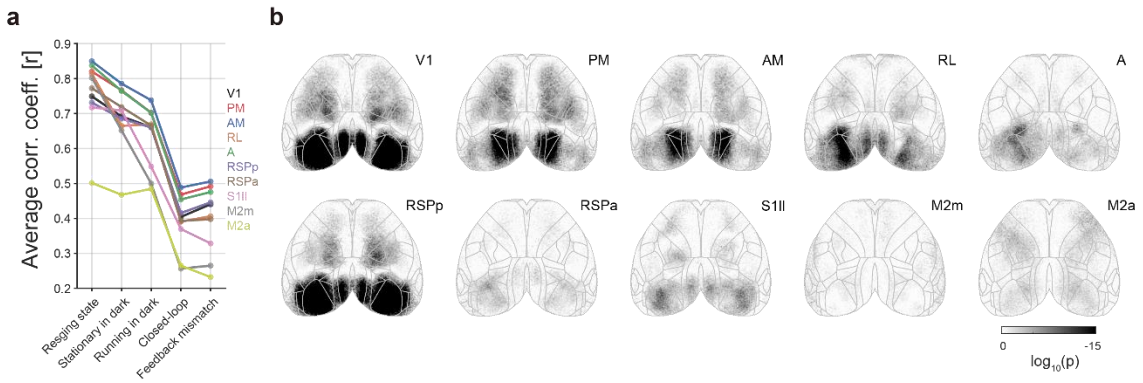

Supplementary Figure 8: Correlation coefficient during different contexts periods

(a) Average Pearson's correlation coefficient [r] between each ROI and the other nine ROIs ($p < 0.01$, Kruskal−Wallis test, related to Fig. 4A)

(b) P-values of statistical test (comparison of two correlation coefficients, two-tailed) of correlation maps (closed-loop vs. mismatch period) in each pixel (related to Fig. 4B)

Fig.S9

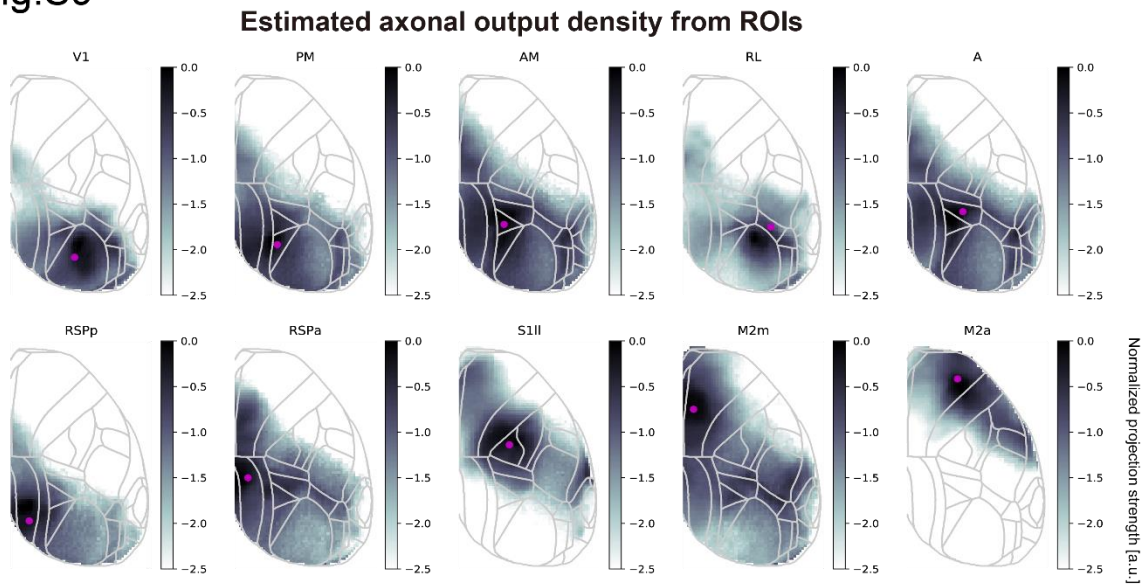

Supplementary Figure 9. Cortico–cortical output connectivity

The normalized output density maps of each area. Magenta dots indicate the position of ROIs. Data used for this analysis were from the database of the Allen Institute Connectivity Atlas.

Table 1:

	V1	PM	AM	RL	A	RSPp	RSPa	S1ll	M2m	M2a
Intercept	0.5349	0.8778	0.9857	0.7399	0.9036	0.8547	0.8986	0.5453	0.5672	0.5972
Speed	< 0.0001	< 0.0001	0.0018	0.6987	0.8627	0.0182	0.2490	0.5382	0.9659	0.5884
ΔSpeed	0.9493	0.2186	0.0253	0.1421	0.0016	0.2667	0.0023	0.0256	0.0278	0.9377

(*p*-value presented in each valuable and area)

Supplementary Table. 1. The effect of locomotion speed and locomotion speed change to mismatch response magnitudes in each area.

Table. 2

Group	Genotype	Virus.	Figures
Random timing mismatch	C57BL/6	AAV-PHP.eB-CaMKII-jGCaMP7f	1C-G, 2C-J, 3A-B, 6A-C, S2A-B, S4A-B, S5, S8, Table 1
Random timing mismatch (Negative control)	C57BL/6	AAV-PHP.eB-hSyn-GFP	S6
Histology	C57BL/6	AAV-PHP.eB-CaMKII-jGCaMP7f	1A-B
Histology (tracing)	C57BL/6	RVΔG-GFP	S3
Semi closed-loop mismatch (Normal experienced)	C57BL/6	AAV-PHP.eB-CaMKII-jGCaMP7f	1E-G, 4D-J, 5B-D, 6D, S4A-B, S7
Semi closed-loop mismatch (Mismatch experienced)	C57BL/6	AAV-PHP.eB-CaMKII-jGCaMP7f	1E-G, 4D-J, 6D, S4A-B, S7

Supplementary Table. 2. Groups of mice and virus vectors used in experiments.

Supplementary Movie 1.

Wide-field imaging of a resting-state mouse.

Top left: the time-lapse of ΔF/F processed from raw fluorescent signals. Gaussian filtering was not performed. Top right: A face movie of an anesthetized mouse. Bottom left: a raw fluorescent movie acquired at 470-nm excitation. Bottom right: a raw fluorescent movie acquired at 405-nm excitation.

Supplementary Movie 2.

A movie of a mouse running in VR.

A head-fixed mouse is running on a treadmill in VR

Supplementary Movie 3.

A movie of a mouse running under the closed-loop condition.

Brain activity, facial image, eye cropped image, pupil size, eye position, and running speed were displayed. Magenta arrows indicate mismatch onset.

Supplementary Movie 4.

A trial average movie of mismatch activities across cortical areas.

Mismatch responses were recorded with wide-field Ca2+ imaging from jGCaMP7f-expressing mice.

Supplementary Movie 5.

A movie of a mouse at a stationary state in the dark.

Brain activity, facial image, eye cropped image, pupil size, eye position, and running speed were displayed.

Supplementary Movie 6.

A movie of a mouse actively running in the dark.

Brain activity, facial image, eye cropped image, pupil size, eye position, and running speed were displayed.